The Pennsylvania State University

The Graduate School

Department of Meteorology

NORTHERN HEMISPHERIC FLOOD FINGERPRINTS

A Thesis in

Meteorology

by

Kathleen Elizabeth-Marie Walls

Submitted in Partial Fulfillment
of the Requirements
for the Degree of

Master of Science

May 2009

The thesis of Kathleen Elizabeth-Marie Walls was reviewed and approved* by the following:

Hampton N. Shirer
Associate Professor of Meteorology
Associate Head of the Department of Meteorology
Thesis Co-Advisor

Paul G. Knight
Senior Lecturer
Pennsylvania State Climatologist
Thesis Co-Advisor

George S. Young
Professor of Meteorology

Sue Ellen Haupt
Senior Research Associate
Associate Professor of Meteorology

William Brune
Professor of Meteorology
Head of the Department of Meteorology

*Signatures are on file in the Graduate School

ABSTRACT

Heavy rain events, which often lead to flooding, affect millions of people every year. The heavy rain-producing synoptic patterns that cause flooding share common configurations, or fingerprints. Obliquely rotated Empirical Orthogonal Functions Analysis reveals six different mid-latitude Northern Hemispheric synoptic patterns that cause heavy rain events. These Empirical Orthogonal Functions are based on the spatial correlations of the standardized anomalies of four atmospheric fields: 850 hPa zonal wind component, 700 hPa meridional wind component, precipitable water, and mean sea level pressure. Ultimately, identification of the primary synoptic patterns may lead to better flood forecasts and to reduction of life and property loss.

TABLE OF CONTENTS

LIST OF FIGURES

LIST OF TABLES

ACKNOWLEDGEMENTS

I would like to express my sincere gratitude to my advisers, Paul Knight and Nels Shirer, and to my other committee members, George Young and Sue Ellen Haupt, for their support and direction. I want to acknowledge Rich Grumm for his assistance using different datasets, Sonya Miller for her computer programming knowledge, Joe Thompson for his help making WSI graphics, and the Pennsylvania State Climatology Office for helping to find flooding events. I thank my mom, Linda, for her never-ending support, and my dad, who I know would be proud of me today. Without my friends and family, none of this would have ever been possible - Thank you.

Chapter 1

Introduction

Flooding causes billions of dollars in damage every year across the Northern Hemisphere. The synoptic-scale weather patterns creating the heavy rain events that cause flooding share common configurations, or fingerprints. Using strong point analysis, Root et al. (2007) demonstrate that there are repeatable atmospheric fingerprints for mid-Atlantic United States flooding events. Based on this work, we hypothesize that there are common fingerprints not only for mid-Atlantic floods, but also for floods across the mid-latitudes of the Northern Hemisphere.

Multiple cases from the mid-latitudes of the Northern Hemisphere, 20ºN to 60ºN, for which over 2 inches (~50 millimeters) of rain fell in an 18-hour period are evaluated using obliquely rotated Empirical Orthogonal Functions (EOFs). These functions are based on the spatial correlations of the standardized anomalies of four atmospheric fields: 850 hPa zonal wind component U, 700 hPa meridional wind component V, precipitable water PWAT, and mean sea level pressure SLP. The maps, given by the first six EOFs, may be interpreted as different synoptic patterns driving Northern Hemispheric heavy rain events.

1.1 Flood Criteria

The American Meteorological Society (AMS) defines “flood” as “the overflowing of the normal confines of a stream or other body of water, or the accumulation of water over areas that are not normally submerged” (Glossary of Meteorology, 2ed). The AMS further identifies “flash

flood" as "a flood that rises and falls quite rapidly with little or no advance warning, usually as the result of intense rainfall over a relatively small area. Some possible causes are ice jams, dam failure, and topography" (IBID). Although the National Weather Service (NWS) *Glossary of Hydrologic Terms* provides a similar definition of "flood," the NWS glossary defines a "flash flood" on a specific time scale as "a flood which follows within a few (usually less than six) hours of heavy or excessive rainfall…"

Because flood criteria are not uniform across the scientific community, we are motivated by the NWS "flash flood" definition and define "flood" as the rise of water owing to excessive rainfall that is greater or equal to 2 inches (~50 mm) within an 18-hour period.

1.2 Flooding Events

Flooding events come from four sources, spanning 1979 to 2007. We obtain flooding events from the National Climate Data Center event database from 1979 to 2007, the CPC MORPHing technique CMORPH from 2002 to 2007, the China Meteorological Administration from 1979 to 2007, and the *Encyclopedia Britannica* disaster articles from 1979 to 1999. These sources provide an estimated date, time, and initial location for case analysis. These four sources yield 322 events from North America, Europe, and Asia that are then validated using Japanese 25-year Reanalysis (JRA25) data, as described in section 1.2.1.

1.2.1 Evaluating Cases Using the JRA25 Dataset

Reliable surface rainfall totals are not available for flood cases outside of North America; thus, an objective method for assessing the likely rainfall amount is needed. Because its performance of global precipitation is the best among other reanalyses, the Japanese 25-Year

Reanalysis (JRA25) is used to evaluate rainfall totals (Onogi et al. 2007). Six-hour global total precipitation distribution and amount are reproduced well both in space and time in this dataset (IBID). The JRA25 is projected on a 1.125º X 1.125º horizontal grid. Its fine grid resolution allows usable approximations of the exact time and location of the flooding event.

The Grid Analysis and Display System GrADS possesses an algorithm that assists in locating where and in what specific 6-hour time period the heaviest rainfall occurred, based on an estimated time of occurrence from the flood database. The rainfall amounts juxtaposed to the 6-hour time period of heaviest rainfall then are calculated, thereby providing the total rainfall for an 18-hour period.

Although ground truth data is available for North America, it does not share the same spatial and temporal characteristics as the JRA25 data. North American cooperative network (COOP) reports provide a 24-hour rainfall total for a specific point in North America. JRA25, on the other hand, averages a 6-hour rainfall total over a 1.125º X 1.125º grid box. Because similar spatial and temporal characteristics are necessary, COOP cannot be used to validate the use of JRA25 rainfall estimates.

1.2.2 Case Selection

The JRA25 is used to determine the flooding events in which 2 or more inches (~50 mm) of rain fell in an 18-hour period. Two hundred quality controlled events from North America, Europe, and Asia that met these criteria are selected for the analysis. Figure 1.1 displays the locations of the 200 cases selected. There are 33 cases located in North America, 38 located from the Azores to the Middle East, and 129 located in eastern Asia.

To assess which synoptic patterns are prominent in what area in Chapter 4, we divide the Northern Hemisphere into three regions: West Coast, Central Continent, and East Coast. The

region identified as “West Coast” includes events from the western United States between the longitudes of -123º and -117º and western Europe between the longitudes of -9º and 27º. The event that occurred in the Azores at -28º longitude is included in this category. “Central Continent” includes the central United States between the longitudes of -112º to -85º, together with eastern Europe and the Middle East between the longitudes of 31º to 77º. The region considered “East Coast” includes the eastern third of the United States between the longitudes of -85º and -72º, and Asia between the longitudes of 102º and 141º.

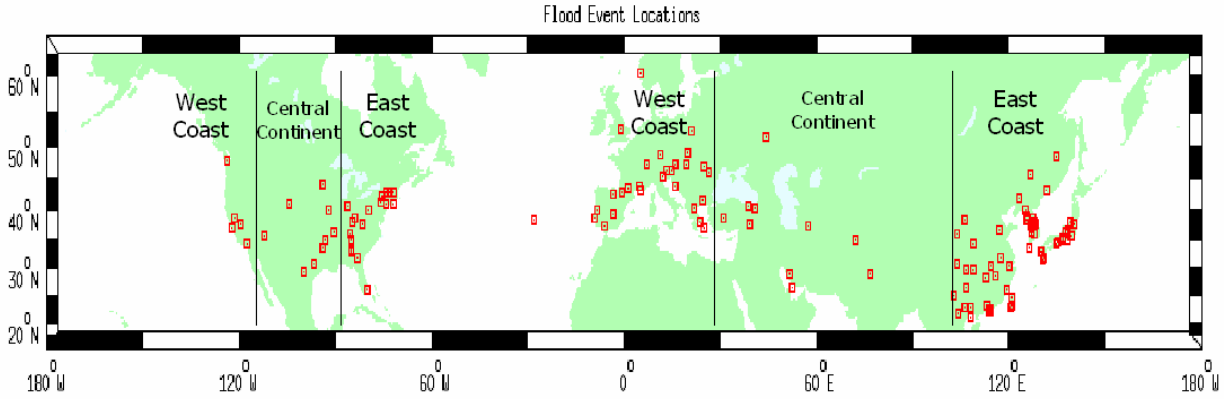

Figure 1.1. Location of 200 cases selected across the mid-latitudes of the Northern Hemisphere in which 2 or more inches of rain fell in an 18-hour period spanning 1979 to 2007. The events are divided into three regions: West Coast, Central Continent, and East Coast.

Chapter 2

Extraction of Four Atmospheric Variables

For each case, the 850 hPa zonal wind component U, 700 hPa meridional wind component V, precipitable water PWAT, and mean sea level pressure SLP values are retrieved from the NCEP-NCAR Global Reanalysis GR dataset. To mitigate the effects of seasonal variation in the values, we calculate standardized anomalies SA of these four atmospheric variables. We use the GR dataset, because of its accessibility and incorporated climatology, which facilitates the calculation of standardized anomalies.

In combination, 850 hPa U-wind, 700 hPa V-wind, PWAT, and SLP best describe the synoptic setup of heavy rainfall events (Maddox et al. 1979; Jessup and DeGaetano 2008). Maddox et al. (1979) use a variety of factors, including wind data at multiple levels, to determine the meteorological conditions necessary for flooding events in the United States. Because we are interested particularly in low-level moisture and temperature advection, our paper uses low-level wind components from the 700 hPa and 850 hPa levels. Maddox et al. (1979) find that all floods in their study possess a large amount of moisture through a deep tropospheric layer. Thus, precipitable water PWAT is included in our analysis, and is defined as the amount of liquid water in a vertical column extending from the surface to 300 hPa, measured in kg/m^2. Advancing low pressure systems often facilitate and amplify the lift needed to produce heavy rainfall; therefore, mean sea level pressure SLP is the fourth and final component.

2.1 NCEP/NCAR Global Reanalysis Dataset

The NCEP/NCAR Global Reanalysis GR dataset is used to determine the 850 hPa U-wind, 700 hPa V-wind, precipitable water, and mean sea level pressure values for each event. The GR dataset is available at four daily times (00 UTC, 06 UTC, 12 UTC, and 18 UTC), beginning in 1948 and extending to the present. The dataset includes 17 vertical pressure levels on a horizontal spatial resolution of 2.5º by 2.5º (Kalnay et al. 1996).

Using GrADS, we excerpt GR values for the four atmospheric fields for a 9 by 9 array of grid point values centered on the flood event. Use of this synoptic-scale grid spanning 22.5º by 22.5º captures only the primary synoptic pattern.

2.2 Calculation of Standardized Anomalies

As in the work of Root et al. (2007), the goal of our research is to identify anomaly patterns; therefore, a technique similar to that developed by Hart and Grumm (2001) is used to produce and standardize the magnitude of the anomalies of the four atmospheric variables listed in the beginning of this chapter. Standardizing the anomaly fields "preserves both the annual and diurnal cycles while smoothing the irregularities resulting from undersampling of season-to-season variations" (Root et al. 2007). Standardized anomalies SA are calculated at each grid point surrounding the flood even via

$$\mathbf{SA = (V - \mu) / \sigma,} \tag{2.1}$$

where **V** is the atmospheric variable value, **μ** is the mean of the 21-day average centered on the given flood date, and **σ** is the value of one standard deviation given by the most recent (1971-2000) 30-year World Meteorological Organization climatology for that grid point location. Because the standardized anomalies are calculated for a 9 by 9 array of grid points centered on the event, each SA field forms a 9X9 matrix with 81 grid points (Figure 2.1).

	Grid Point	Grid Point	Grid Point	Grid Point	Grid Point	Grid Point	Grid Point	Grid Point	Grid Point
9	1	10	19	28	37	46	55	64	73
8	2	11	20	29	38	47	56	65	74
7	3	12	21	30	39	48	57	66	75
6	4	13	22	31	40	49	58	67	76
5	5	14	23	32	41	50	59	68	77
4	6	15	24	33	42	51	60	69	78
3	7	16	25	34	43	52	61	70	79
2	8	17	26	35	44	53	62	71	80
1	9	18	27	36	45	54	63	72	81
	1	**2**	**3**	**4**	**5**	**6**	**7**	**8**	**9**

Figure 2.1. Each SA field forms a 9X9 matrix with 81 grid points, which are in columns from left to right beginning with grid point 1. The bold numbers represent the SA coordinates surrounding the grid points. The location of the event is located in the center of the matrix at grid point number 41, which is (5,5) on a SA map.

Figure 2.2 displays maps of the four 9X9 SA fields of a heavy rain event that occurred west of Hong Kong, China on 25 June 1985. The event is located at the center of each grid at point (5,5). Red coloring indicates positive anomaly values, and blue coloring indicates negative anomaly values. Positive anomalies of precipitable water are located around and slightly north of the event location (Figure 2.2a). Negative anomaly values of sea level pressure indicate a low pressure center around and slightly north of the heavy rain event (Figure 2.2b). Positive values of 850 hPa U-wind signify westerlies (winds from the west) near and to the south of the flooding event, and negative anomalies indicate easterlies to the north of the flooding event (Figure 2.2c). Southerlies at 700 hPa, indicated by positive anomalies, exist to the north and east of the flood location, while northerlies are to the north and west of the flooding event (Figure 2.2d). Taken together, these anomaly fields suggest that an extratropical cyclone produced the heavy rain event.

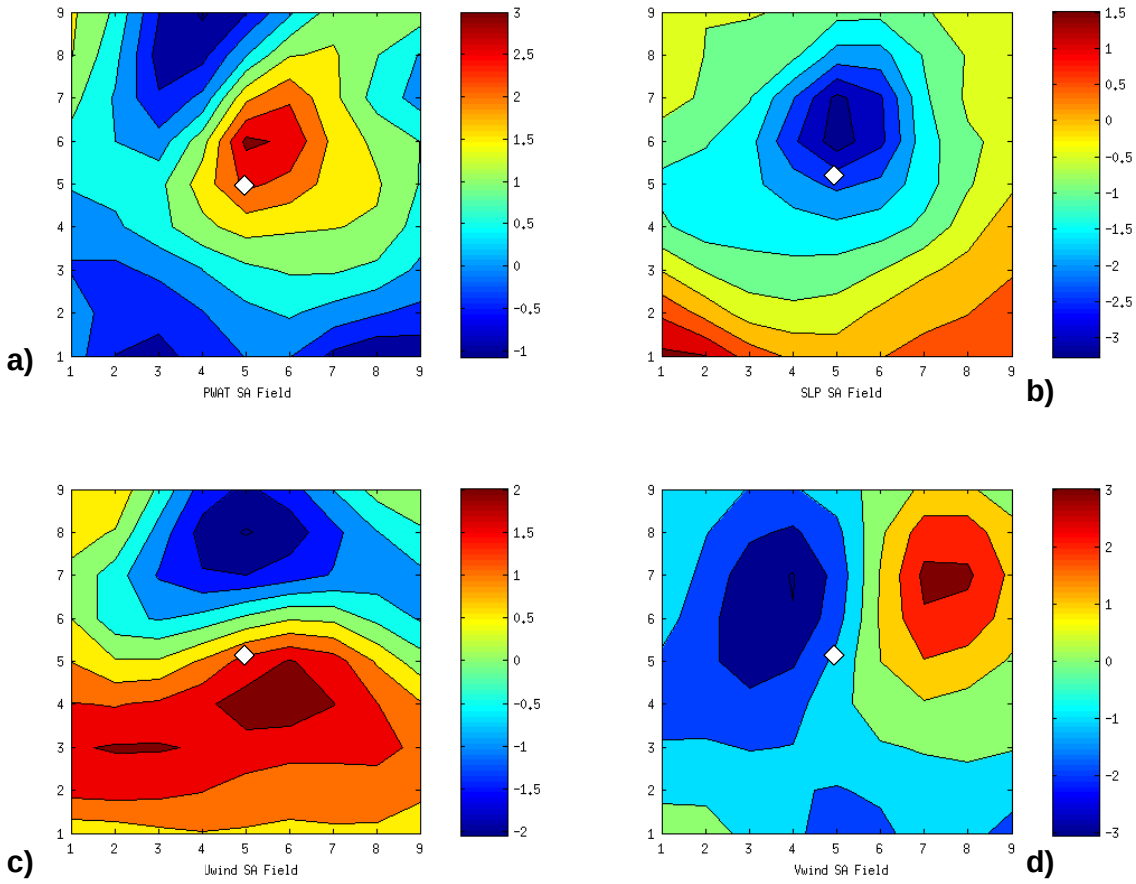

Figure 2.2. The standardized anomaly fields of an event that occurred slightly west of Hong Kong, China on 25 June 1985. The flooding event is denoted by the white diamond located in the center of each grid at (5,5). Here, (a) displays the SA precipitable water PWAT field, (b) displays the SA sea level pressure SLP field, (c) displays the SA 850 hPa U-wind field, and (d) displays the SA 700 hPa V-wind field.

To organize the four SA fields for all 200 events, we combine the data into one 324X200 matrix **D** (Figure 2.3). Four 9X9 SA fields generate 324 SA values for each of the 200 events; therefore, there are 324 rows per column, or event. This 324X200 matrix facilitates the calculation of eigenvectors and eigenvalues in Chapter 3.

Column 1: Event 1	Column 2: Event 2…	…Column 200: Event 200
Row 1: PWAT SA: Grid point 1	**Row 1: PWAT SA Grid point 1**	**Row 1: PWAT SA Grid point 1**
.	.	.
.	.	.
.	.	.
Row 81: PWAT SA Grid point 81	**Row 81: PWAT SA Grid point 81**	**Row 81: PWAT SA Grid point 81**
Row 82: SLP SA Grid point 1	**Row 82: SLP SA Grid point 1**	**Row 82: SLP SA Grid point 1**
.	.	.
.	.	.
.	.	.
Row 162: SLP SA Grid point 81	**Row 162: SLP SA Grid point 81**	**Row 162: SLP SA Grid point 81**
Row 163: 850 U-wind SA Grid point 1	**Row 163: 850 U-wind SA Grid point 1**	**Row 163: 850 U-wind SA Grid point 1**
.	.	.
.	.	.
.	.	.
Row 243: 850 U-wind SA Grid point 81	**Row 243: 850 U-wind SA Grid point 81**	**Row 243: 850 U-wind SA Grid point 81**
Row 244: 700 V-wind SA Grid point 1	**Row 244: 700 V-wind SA Grid point 1**	**Row 244: 700 V-wind SA Grid point 1**
.	.	.
.	.	.
.	.	.
Row 324: 700 V-wind SA Grid point 81	**Row 324: 700 V-wind SA Grid point 81**	**Row 324: 700 V-wind SA Grid point 81**

Figure 2.3. Combination of all SA fields and all events into a 324X200 matrix **D**. There are four 9X9 SA fields per event; thus, each event contains 324 values.

Chapter 3

Empirical Orthogonal Functions

Three of the eigentechniques that have been employed in meteorological research are Empirical Orthogonal Function (EOF) Analysis, Principal Component Analysis (PCA), and Common Factor Analysis (CFA) (Richman 1986). Empirical Orthogonal Functions (EOFs), arguably the most widely used eigentechnique within the meteorological community, are employed here. EOFs basically reduce a dataset to one that contains linear combinations of the original data and that captures the maximum possible variance in the original dataset using the fewest possible combinations. The small set of uncorrelated variables that results is much easier to manipulate and use in further analyses than is a larger set of correlated variables (Dunteman 1989). The original unit-length eigenvectors that constitute the EOFs are rotated both orthogonally and obliquely. The number of eigenvectors to be rotated is determined using a simple scree test (Cattell 1966a). The scree test combined with meteorological knowledge lead to the rotation of six eigenvectors, and therefore, to the production of six EOFs.

3.1 Eigenvector Calculations

Eigenvectors and eigenvalues are calculated using the four atmospheric standardized anomaly SA fields, precipitable water PWAT, sea level pressure SLP, 850 hPa U-wind, and 700 hPa V-wind. The eigenvalue-eigenvector pairs contain the same information as the original SA matrices, and may be regarded as a transformation of the original matrix of the four SA fields

(Wilks 1995). Eigenvectors, **e,** and eigenvalues, λ, are real-valued. Eigenvectors are of unit length, so that the dot product of any eigenvector with itself equals one, as displayed in (3.1):

$$e_i^T e_j = \begin{cases} 1, & i = j \\ 0, & i \neq j \end{cases} \tag{3.1}$$

A function in Matlab performs the determination of eigenvectors and eigenvalues quickly and efficiently by satisfying the equation:

$$\mathbf{Ae} = \lambda\mathbf{e}, \tag{3.2}$$

where an eigenvalue, λ, is a scalar, and an eigenvector, **e**, is a nonzero vector of the square matrix **A**. The square matrix **A** is a 324X324 matrix, composed of standardized anomaly data **D** multiplied by its transpose. It is important to note that if a vector **e** satisfies (3.2), then its negative, **-e**, also will satisfy the equation. This fact is important when interpreting the EOF figures in Chapter 4.

3.2 Unrotated Empirical Orthogonal Functions

Unrotated EOFs offer numerous advantages. The methodology of the EOFs may be applied easily to a dataset without consuming a large amount of time. Richman (1986) explains that the patterns of unrotated EOFs display the maximum variance in a dataset and are unaffected by the number of EOFs retained.

The use of EOFs, or unit-length eigenvectors, was pioneered by Lorenz (1956) and has remained virtually unchanged since that seminal paper. Application of EOFs in this thesis maximizes the variance of the four atmospheric variables, while also taking into consideration the correlations among the four variables at the 81 grid points on the 9 by 9 grid (Chapter 2). This method not only condenses much information, but ensures that patterns created by the EOFs are consistent physically with atmospheric processes (Wilks 1995).

The first unrotated EOF explains the largest percentage of the variance amongst the 200 flooding events, 19.0% (Figure 3.1). The flooding event is located at the center of each grid at point (5,5). Red coloring indicates positive anomaly values, and blue indicates negative anomaly values. Positive anomalies of precipitable water are centered on the event location (Figure 3.1a). Negative anomaly values of sea level pressure indicate a low pressure to the west (left) of the flooding event (Figure 3.1b). Positive values of 850 hPa U-wind signify westerlies (winds from the west) near and to the southwest of the flooding event, while negative anomalies indicate easterlies to the north of the flooding event (Figure 3.1c). Southerlies at 700 hPa, indicated by positive anomalies, exist in the eastern two-thirds of the grid, including the area around the flooding event; northerlies are located to the northwest of the event location (Figure 3.1d). The configuration of these fields suggests a pattern like that of an extratropical cyclone.

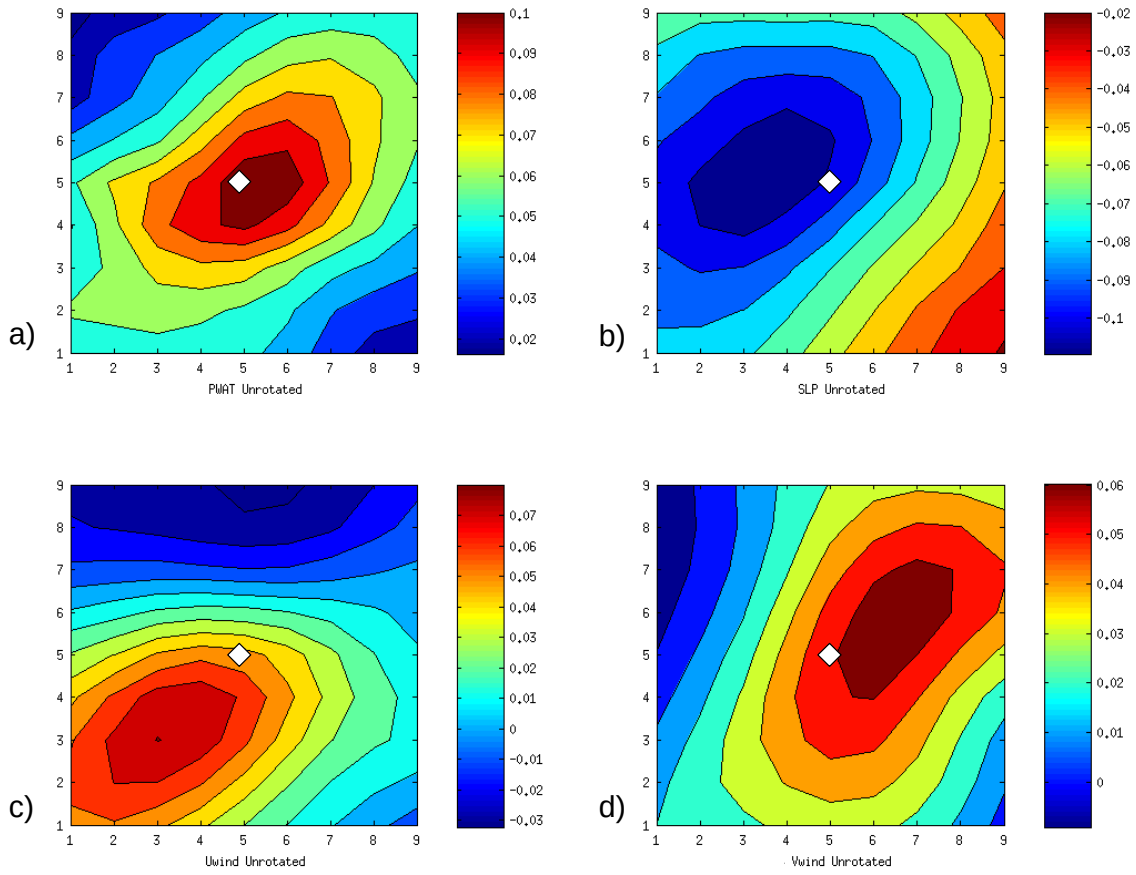

Figure 3.1. The first unrotated EOF. The flooding event is located in the center of each grid at (5,5), indicated by the white diamond. Here, (a) displays the precipitable water PWAT field, (b) displays the sea level pressure SLP field, (c) displays the 850 hPa U-wind field, and (d) displays the 700 hPa V-wind field.

3.3 Rotated Empirical Orthogonal Functions

Although unrotated EOFs offer many advantages, there are several disadvantages that hinder the ability of unrotated EOFs to display the synoptic patterns that cause significant flooding events. Richman (1986) explains in detail why rotating EOFs allows for a better analysis of meteorological data. Rotation minimizes the effect of domain shape dependence. Unrotated EOFs depend heavily on the domain shape, or the geometry of the domain. The geometry, in this case, influences the resulting pattern and obscures the underlying physics. A similar issue exists

when subdividing the domain. Basically, unrotated EOFs obtained for a large domain become compressed to fit a specific subdomain region and so do not explicitly explain the pattern within that subdomain. Rotated solutions, however, are less influenced by domain and subdomain restrictions. Richman (1986) continues that unrotated solutions suffer from large sampling errors when the eigenvalues of a dataset are close numerically. He concludes his argument by stating that underlying correlation fields are depicted properly by rotated EOFs, and meteorological patterns become clearer when applying rotation, as noted in Chapter 4.

A scree test is performed to determine how many eigenvectors, or factors, to rotate (Figure 3.2). The scree test, proposed by Cattell (1966a), plots the eigenvalues in descending order of magnitude against their factor number. The point at which the tail of the plot becomes linear, where eigenmodes represent random noise, is where no further physical meaning is attained (Wilks 1995). Circled in red is the area where the eigenvalue variation becomes linear, or where the random noise begins. According to this plot, fewer than 25 factors account for the majority of the variance. To obtain a more precise answer, we calculate the number of factors that captures 90% of the variance. Twenty-four factors account for 90.2% of the variance.

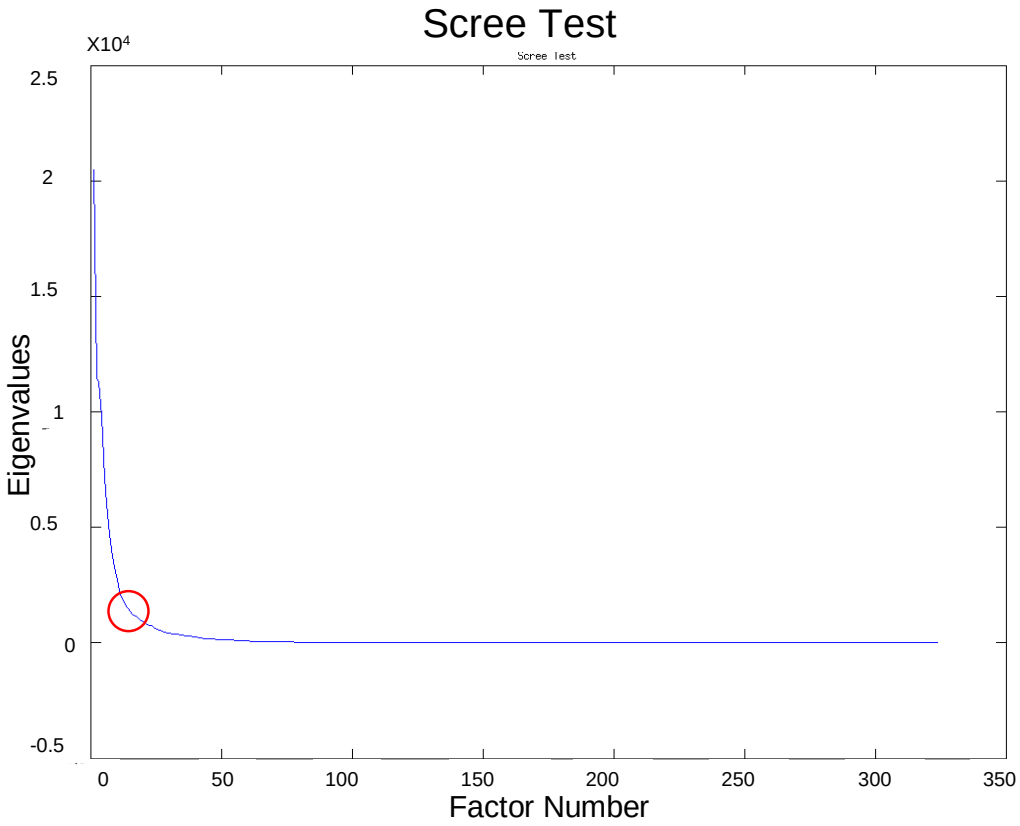

Figure 3.2. A scree test is performed to determine where to stop extracting eigenmodes. The red circle indicates the area where the eigenvalues become linear. All eigenmodes beyond this area may be regarded as random noise and no further physical information may be attained.

The goal is to rotate the fewest number of factors, while still explaining as much variance as possible through the patterns of the retained EOFs. After careful analysis of the EOFs produced by rotating one through 24 factors, we find that the rotation of six factors reveals the most meteorologically meaningful patterns and explains 61.4% of the variance amongst the 200 events. It is important to note that unlike the unrotated EOFs, the first rotated EOF does not necessarily explain the largest variance; the total variance explained, 61.4%, is preserved amongst the six regardless of rotation, however. We next perform and compare orthogonal and oblique rotations on these six EOFs.

3.3.1 Orthogonally Rotated EOFs

Orthogonal rotation basically means rotating the original unit-length eigenvectors to a new set of coordinate axes that are perpendicular to one another (Dunteman 1989). The new coordinate axes are defined by their correlation with the original data, as are the unrotated EOFs. The rotated eigenvectors are a linear transformation of the first six original unit eigenvector sets,

$$\tilde{\mathbf{E}} = \mathbf{ET}, \tag{3.3}$$

where **E** is a 324X6 matrix of the first six unit-length eigenvectors, **T** is a 6X6 rotation matrix, and $\tilde{\mathbf{E}}$ denotes the 324X6 matrix of rotated eigenvectors (Wilks 1995). The rotation matrix **T** is orthogonal in the case of orthogonal rotation:

$$\mathbf{TT}^{\mathrm{T}} = \mathbf{I}, \tag{3.4}$$

where **I** is the identity matrix that consists of ones on the diagonal and zeros elsewhere. Thus, the resulting rotated eigenvectors are mutually perpendicular and are of unit length (Wilks 1995).

A function in Matlab is used to perform the rotation of the first six eigenvectors, or factors, by maximizing the Varimax criterion (Kaiser 1958). This criterion maximizes the sum of the variances of the squared rotated eigenvector elements in order to achieve simple structure, which is explained in section 3.3.3.

The third orthogonally rotated EOF displays a pattern resembling the open stage of a classic Norwegian Cyclone (Figure 3.3) (Petterssen 1941). A strong low in the southeastern quadrant of the domain in blue color (Figure 3.3b) creates significant low-level positive vorticity that can be seen by the distinct counter-clockwise circulation of the winds aloft. The 700 hPa V-wind (Figure 3.3d) shows southerly flow in red color in the southeast portion of the domain with vigorous northerly flow in blue color across the central and southwestern parts of the domain. The 850 hPa U-wind (Figure 3.3c) indicates an easterly flow in blue color in the north-central portion of the map and a strong westerly flow in red in the southern part of the domain. Finally,

precipitable water (Fig. 3.3a) is greatest on the eastern side of the low in red color, where the moisture from the south is the greatest.

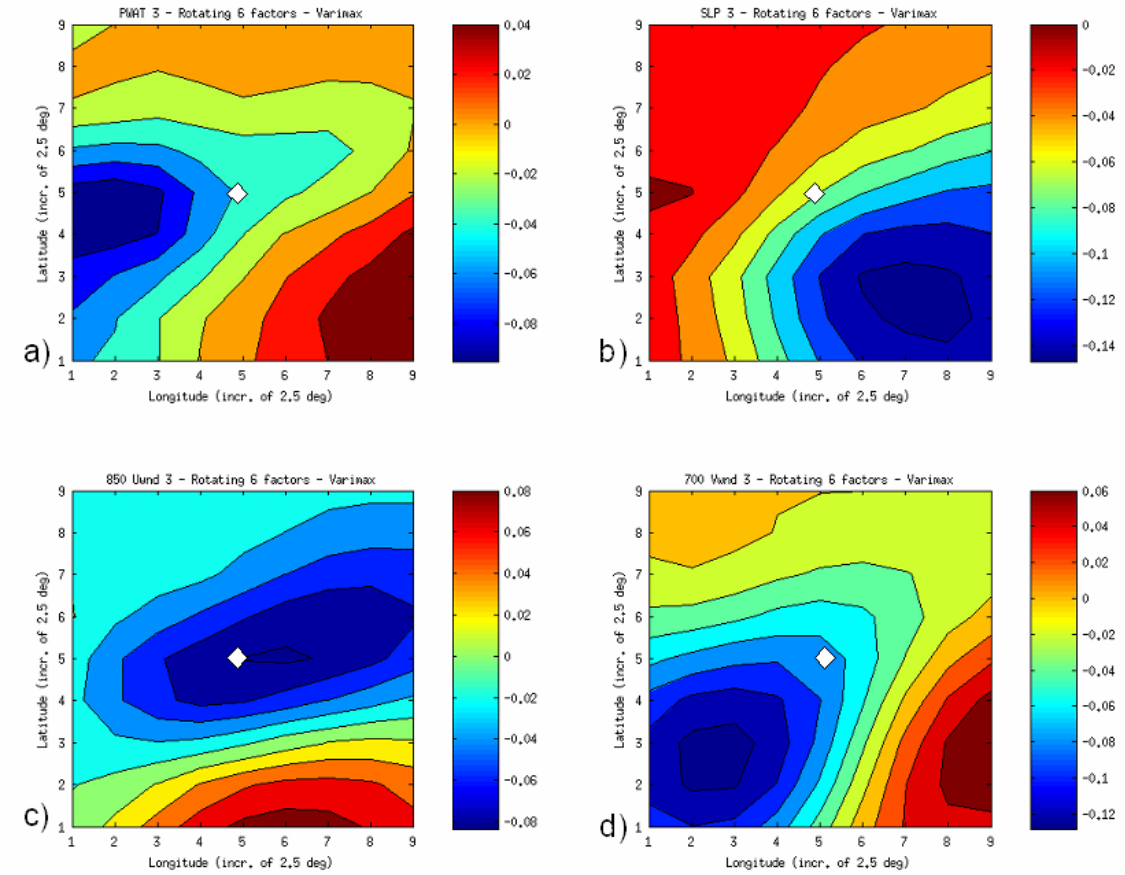

Figure 3.3. The third orthogonally rotated EOF describing a pattern similar to the open stage of a Norwegian Cyclone. The flooding event is located in the center of each grid at (5,5), indicated by the white diamond. Here, (a) displays the precipitable water PWAT field, (b) displays the sea level pressure SLP field, (c) displays the 850 hPa U-wind field, and (d) displays the 700 hPa V-wind field.

3.3.2 Obliquely Rotated EOFs

The six unrotated EOFs are obliquely rotated according to the Promax criterion of Hendrickson and White (1964). The Promax rotation uses an oblique Procrustes transformation, where the Procrustes equation is:

$$\mathbf{B} = \mathbf{ET} + \mathbf{Q}. \tag{3.5}$$

Here, **B** is a 324X6 rotation matrix, **E** is a 324X6 loading elements matrix composed of the first six unit-length eigenvectors, **T** is a 6X6 transformation matrix, and **Q** is a matrix of discrepancies or residuals (Richman 1986). In a Promax solution, **Q** is minimized and assumed to be negligible. This assumption renders (3.3) valid for the oblique rotation as well as the orthogonal rotation. The orthogonal solution usually is close to an optimum oblique solution; therefore, functions of the loading elements of an orthogonal solution are used to construct oblique EOFs (Richman 1986).

Considering that orthogonal rotation loading elements are included within the Promax rotation, it is not surprising that the interpretation of the third EOF rotated according to Promax criterion (Figure 3.4) is nearly identical to that of the Varimax solution (Figure 3.3). The interpretation of an open stage of a Norwegian cyclone is, again, applied. Although the wind fields in the oblique rotation are nearly identical to those of the orthogonal rotation, minor differences between the two rotations exist. PWAT is slightly higher over the flooding event in the orthogonal rotation. In the SLP field, there is more high pressure building to the northeast of the low in the oblique solution.

Richman (1986) uses different methods of rotation in a Monte Carlo simulation to determine which rotations perform the best. He writes that Promax is the "most accurate widely available solution" and that Varimax "does not fare as well" (Richman 1986). Although the two rotations are visually similar, Richman (1986) determines that the Promax rotation is one of the

most accurate in recovering the input structure of the modes of variation; therefore, we use the Promax solutions to best represent the synoptic patterns analyzed in Chapter 4.

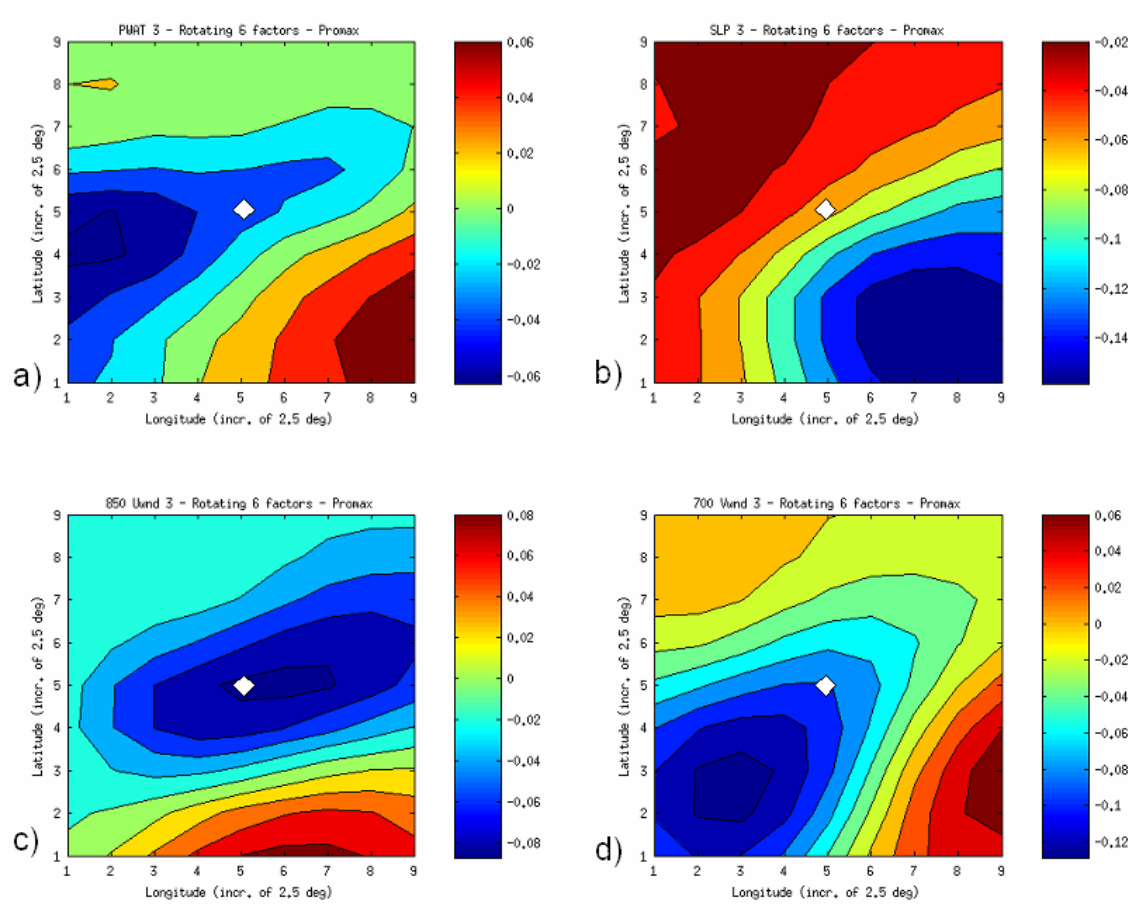

Figure 3.4. The third obliquely rotated EOF describing a pattern similar to the open stage of a Norwegian Cyclone. Although the wind fields in the oblique rotation are nearly identical to those of the orthogonal rotation, minor differences between the two rotations exist in the PWAT and SLP fields. The flooding event is located in the center of each grid at (5,5), indicated by the white diamond. Here, (a) displays the precipitable water PWAT field, (b) displays the sea level pressure SLP field, (c) displays the 850 hPa U-wind field, and (d) displays the 700 hPa V-wind field.

3.3.3 Simple Structure

To help ensure that the rotated matrix is easily interpretable, Thurstone (1947) develops a set of requirements that he calls simple structure. The concept underlying simple structure is to

explain the maximum amount of variance in each flooding event using the smallest number of EOFs (Richman 1986).

To determine the simple structure values, event scores are first calculated using a least-squares approach:

$$(\tilde{\mathbf{E}}^{\mathrm{T}}\,\tilde{\mathbf{E}})^{-1}\,(\tilde{\mathbf{E}}^{\mathrm{T}}\mathbf{D}) = \mathbf{S}_{\mathbf{rot}}, \tag{3.6}$$

where $\mathbf{D}$ is the matrix of the original SA data, $\mathbf{S}_{\mathbf{rot}}$ is the matrix of the rotated scores, and $\tilde{\mathbf{E}}$ is the original matrix of eigenvectors $\mathbf{E}$ multiplied by the rotation matrix $\mathbf{T}$. (For a full derivation, see Appendix B.) Each event has one score for each EOF for a total of six scores. Scores are used to determine which synoptic pattern(s) best describe each event in section 4.2.

For each event, the simple structure is computed by finding the largest absolute-valued score and dividing it by the sum of the six absolute-valued scores:

$$\textbf{Simple Structure} = \max\left(|\mathbf{S}_{\mathbf{rot}}|\right) / \operatorname{sum}\left(|\mathbf{S}_{\mathbf{rot}}|\right). \tag{3.7}$$

The closer the simple structure value is to 1, denoting perfect simple structure, the closer the event is to being explained by only one of the six EOFs. When the simple structure value is close to 0, then more than one EOF is necessary to explain that event. The values of the simple structures for the 200 flooding events range from 0.22 to 0.62 with a mean of 0.35, indicated by the solid red line (Figure 3.5). Because the simple structure values are not near 1 for any case, we conclude that all of the 200 cases are explained by a combination of the six EOFs and not by a single EOF. Thus, all six EOFs are necessary to interpret the meteorology underlying each flooding event.

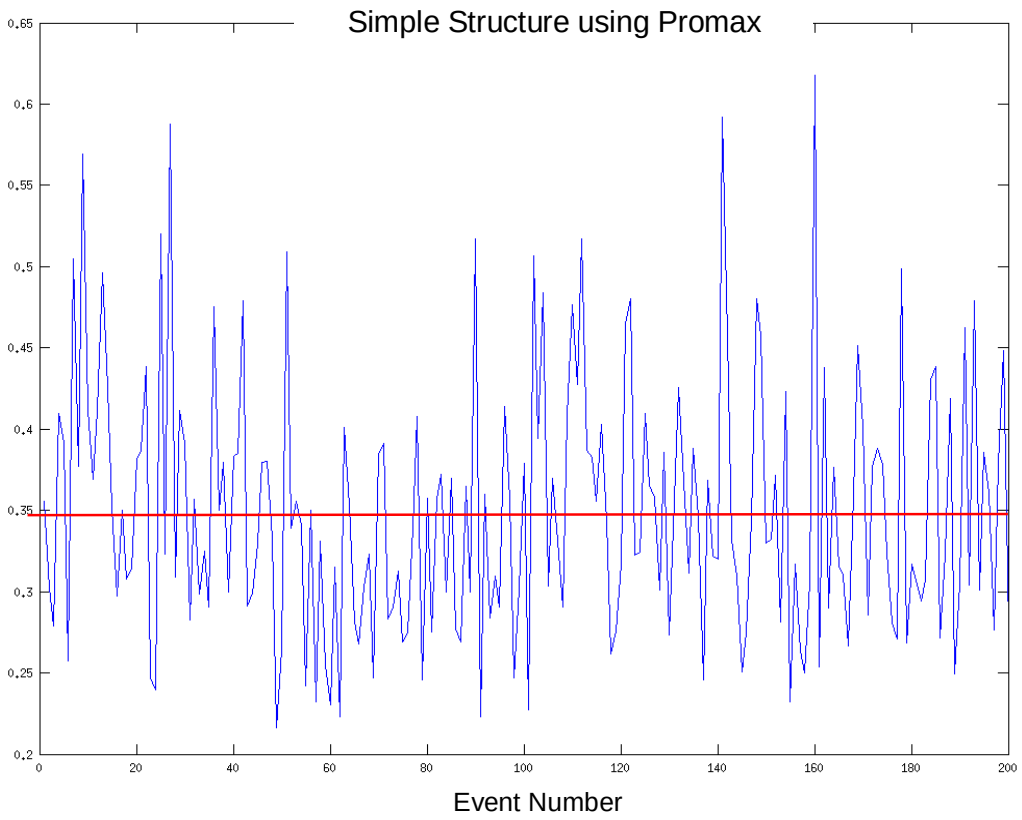

Figure 3.5. Simple structure using Promax criterion. The mean of the simple structures for the 200 flooding events is 0.35, indicated by the solid red line. Because the simple structure values do not equal 1, we conclude that these cases are explained by a combination of EOFs.

Chapter 4

Results of Six-Factor Oblique Rotation

One of the most important characteristics of oblique EOF rotation is that rotated solutions yield more meteorologically significant results (Richman 1986). Each EOF that we obtain may be interpreted as a synoptic pattern that causes excessive rainfall and leads to flooding. Because six factors are rotated, six synoptic patterns are revealed that together explain 61.4% of the variance amongst the 200 heavy rain events in this study.

As noted by the simple structure testing in section 3.3.3, scores reveal that events are explained using a combination of EOFs. To categorize which EOFs best explain heavy rain events across the West Coast, Central Continental, and East Coast regions introduced in Chapter 1, we identify the highest score for each event and so determine the primary synoptic pattern that explains that event. The majority of heavy rain events across the mid-latitudes of the Northern Hemisphere are explained by the second and fifth EOFs, whose patterns respectively represent warm front overrunning and an incipient wave on a front.

By multiplying the six rotated EOFs by the six corresponding scores, we reconstruct the standardized anomaly SA fields of the 200 events and calculate a correlation between the reconstructed SA fields and the original SA fields. The average correlation coefficient between the original SA fields and those reconstructed is 0.78, validating our methodology.

4.1 Meteorological Interpretation

Each of the six EOFs may be interpreted as a different, heavy rain producing synoptic pattern. The first EOF (Figure 4.1) represents a cold conveyor belt pattern (Djuric 1994). In a mature cyclone, the cold conveyor belt is located to the north of the warm front and in the cold sector of the cyclone, where layered clouds, like altostratus, tend to be present. These stratiform clouds have the ability to produce significant rainfall totals. Also, terrain effects can enhance lift and augment the potential for a heavy rain event.

The heavy rain event occurs slightly to the southwest of the center of low pressure, where precipitable water is not high and components of winds at 850 and 700 hPa are convergent. Surface low pressure in blue color and its associated low-level convergence dominates the majority of the domain (Figure 4.1b). Southerly winds (winds from the south) in red color on the eastern side of the low and northerly winds in blue color on the western side of the low display positive vorticity at 700 hPa (Figure 4.1d). Winds at 850 hPa are from the west in red on the western side of the low and are from the east in blue on the eastern side of the low (Figure 4.1c), fortifying low-level positive vorticity. Precipitable water is greatest in red to the north of the low in the northern third of the domain, where low-level southeasterly winds steer in moisture (Figure 4.1a). Precipitable water is minimal to the southwest of the low, where “DRY” is written on the schematic. In this area of subsidence, high pressure is located and is reinforced by winds from the north and west at low levels.

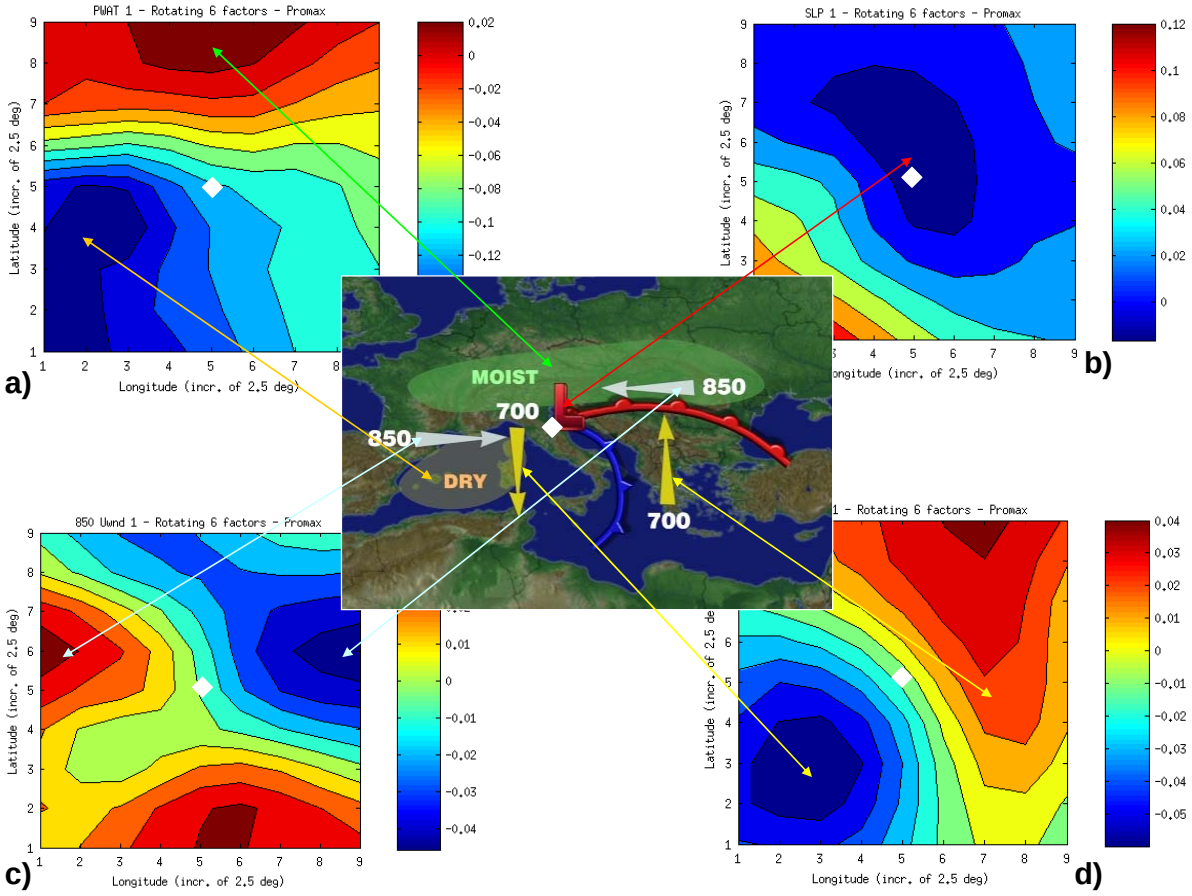

Figure 4.1. The first EOF and its representative synoptic pattern, the cold conveyor belt. The heavy rain event is located in the center of each grid at (5,5). Here, (a) displays precipitable water PWAT, (b) displays sea level pressure SLP, (c) displays 850 hPa U-wind, (d) displays 700 hPa V-wind.

The second EOF represents warm front overrunning (Figure 4.2). The heavy rain event occurs to the northeast of the center of low pressure, where the precipitable water is high and a strong southerly flow at 700 hPa dominates. Surface low pressure indicated in blue extends from the southwestern corner to the north central area of the domain (Figure 4.2b). Precipitable water in red (Figure 4.2a) is greatest along this extended area of low pressure and can be seen on the graphic as moisture along the warm front, driven by strong, southerly winds at 700 hPa in red (Figure 4.2d). There is westerly flow at 850 hPa in red in the southwestern and northeastern quadrants of the domain, and easterly flow in blue in the southeastern and northwestern quadrants of the domain (Figure 4.2c). It is important to note that as in the first EOF, terrain effects can

enhance vertical motion and provide the potential for heavy rain events in the area of warm front overrunning.

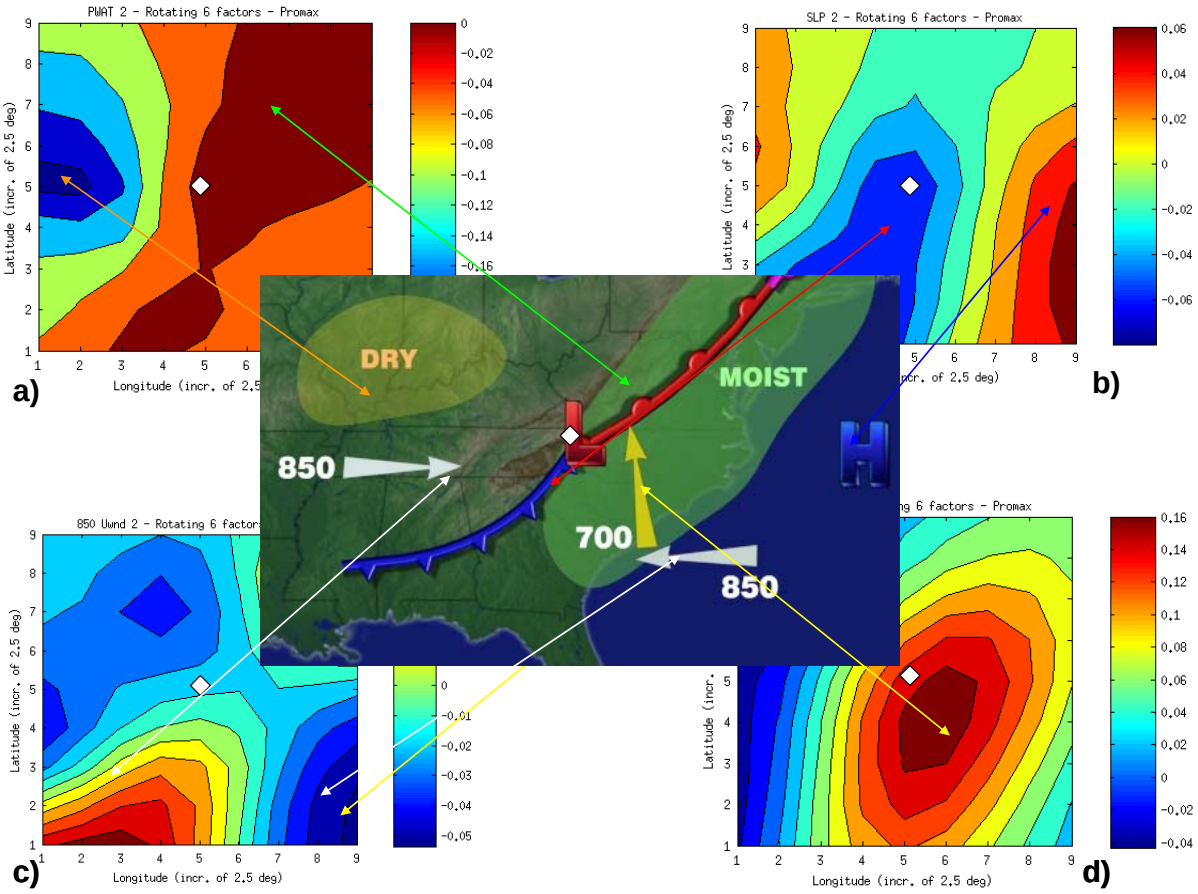

Figure 4.2. The second EOF and its representing synoptic pattern, warm front overrunning. The heavy rain event is located in the center of each grid at (5,5). Here, (a) displays precipitable water PWAT, (b) displays sea level pressure SLP, (c) displays 850 hPa U-wind, and (d) displays 700 hPa V-wind.

Figure 4.3 represents the third EOF that can be interpreted as the open, or developing, stage of a Norwegian Cyclone (Petterssen 1941). A vigorous low in the southeastern quadrant of the domain in blue (Figure 4.3b) creates significant low-level positive vorticity that can be seen by the distinct counterclockwise circulation of the winds aloft. The 700 hPa V-wind (Figure 4.3d) shows southerly flow in red in the southeastern portion of the domain with strong northerly flow in blue across the central and southwestern parts of the domain. The 850 hPa U-wind (Figure

4.3c) indicates an easterly flow in blue in the north central portion of the area and a strong westerly flow in red in the southern part of the domain. Finally, precipitable water (Figure 4.3a) is greatest in red on the eastern side of the low. On the schematic, this moisture-infused area is indicated by an “M”. Precipitable water is the least in the central and western portions of the domain and is indicated by a “D”, representing dry air, on the schematic. Moisture is advected northwestward (towards the northwest) by low-level winds, and there is moisture convergence over the area that experiences the heavy rain.

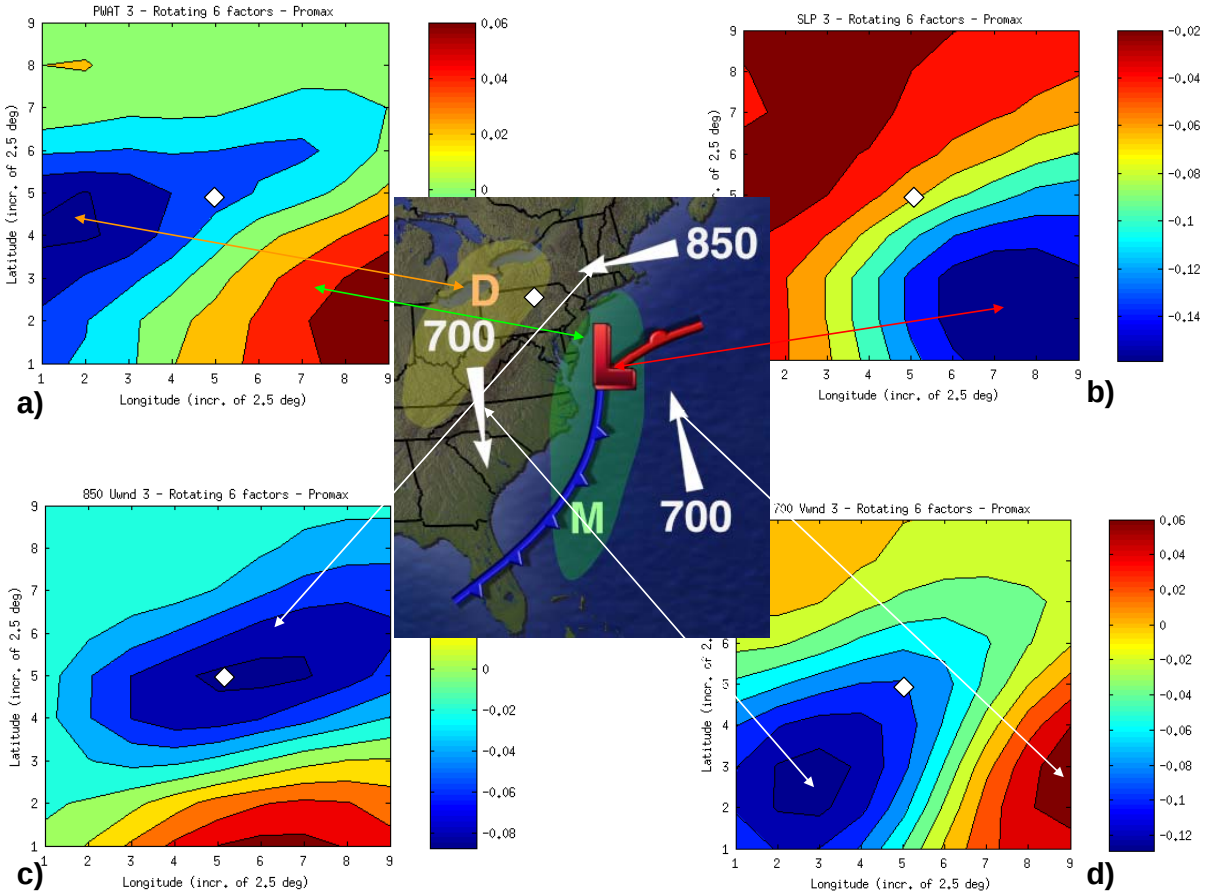

Figure 4.3. The third EOF and its representing synoptic pattern, the open, or developing, stage of a Norwegian Cyclone. The heavy rain event is located in the center of each grid at (5,5). Here, (a) displays precipitable water PWAT, (b) displays sea level pressure SLP, (c) displays 850 hPa U-wind, and (d) displays 700 hPa V-wind. On the schematic "M" represents moist air, which is high in precipitable water, and "D" represents dry air, which lacks precipitable water.

The fourth EOF represents an upsloping pattern (Figure 4.4). The heavy rain event is to the northeast of the surface low, in an area of high precipitable water, easterlies at 850 hPa, and southerlies at 700 hPa. In this area, terrain enhances vertical motion, or lift, and increases the potential for heavy rain. Surface high pressure in red is to the north of the heavy rain event, and surface low pressure in blue is to the south of the heavy rain event (Figure 4.4b), creating an area of strong easterlies at 850 hPa in blue (Figure 4.4c) in the northern half of the domain. Easterly flow is juxtaposed with an area of high precipitable water located over and slightly to the west of the heavy rain location, and is indicated on the schematic by "MOIST". The easterly winds in

combination with southerly winds at 700 hPa in red (Figure 4.4d) help to drive the high moisture to the northwestern side of the low.

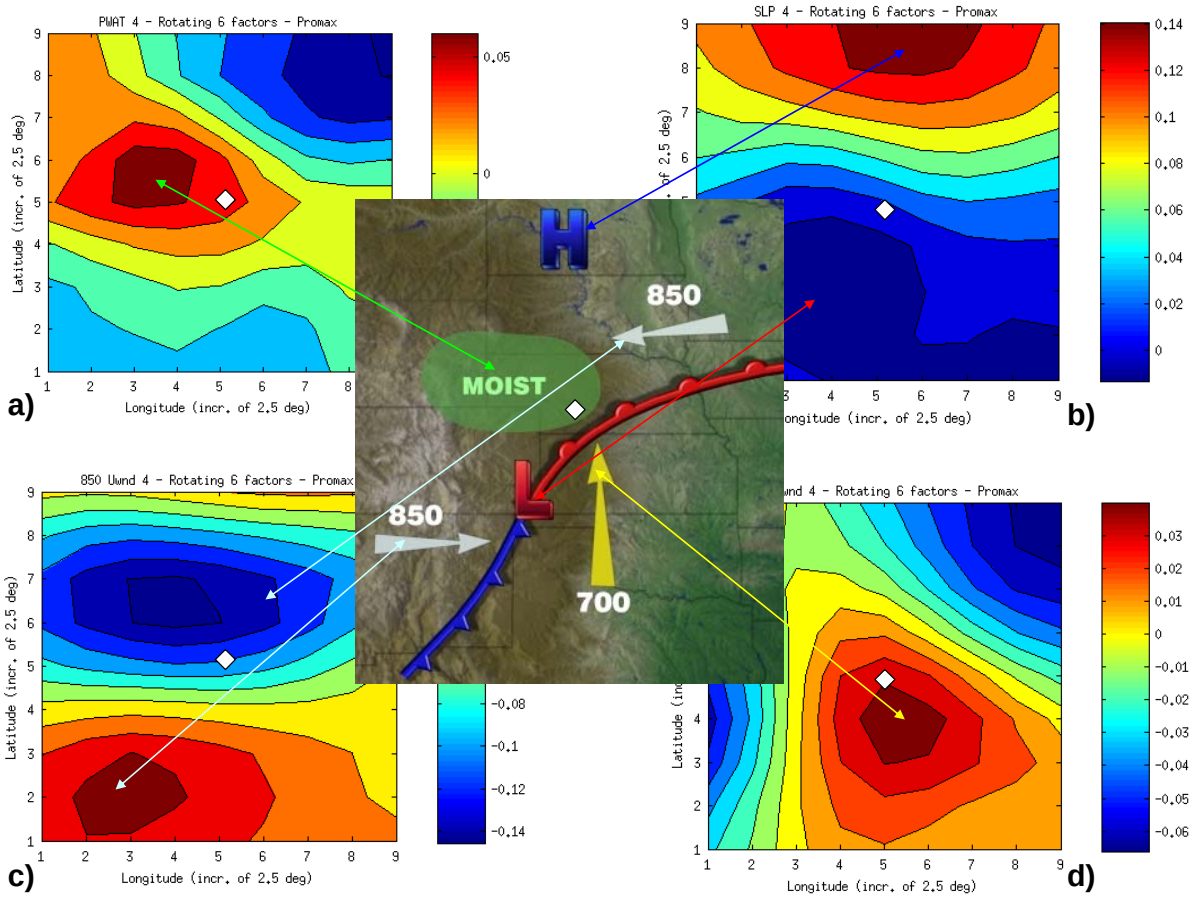

Figure 4.4. The fourth EOF and its representing synoptic pattern, upsloping. The heavy rain event is located in the center of each grid at (5,5). Here, (a) displays precipitable water PWAT, (b) displays sea level pressure SLP, (c) displays 850 hPa U-wind, and (d) displays 700 hPa V-wind.

The fifth EOF represents an incipient wave on a front (Figure 4.5). The heavy rain event is centered over surface low pressure, high precipitable water, westerly winds at 850 hPa, and mild southerlies at 700 hPa. A strong low pressure center in blue (Figure 4.5b) creates convergence and low-level positive vorticity that can be seen by counterclockwise movement of winds at 700 hPa and 850 hPa. To the south of the surface low resides an equally strong surface

high in red, causing westerly winds at 850 hPa in red to dominate in the southern half of the domain (Figure 4.5c). Easterlies at 850 hPa in blue exist to the north of the low. Winds are from the south at 700 hPa in red on the eastern side of the low, and winds are from the north in blue on the western side of the low (Figure 4.5d). High precipitable water in red resides around and slightly to the west of the surface low, where strong westerlies facilitate the zonal orientation of high precipitable water denoted by green on the schematic (Figure 4.5a).

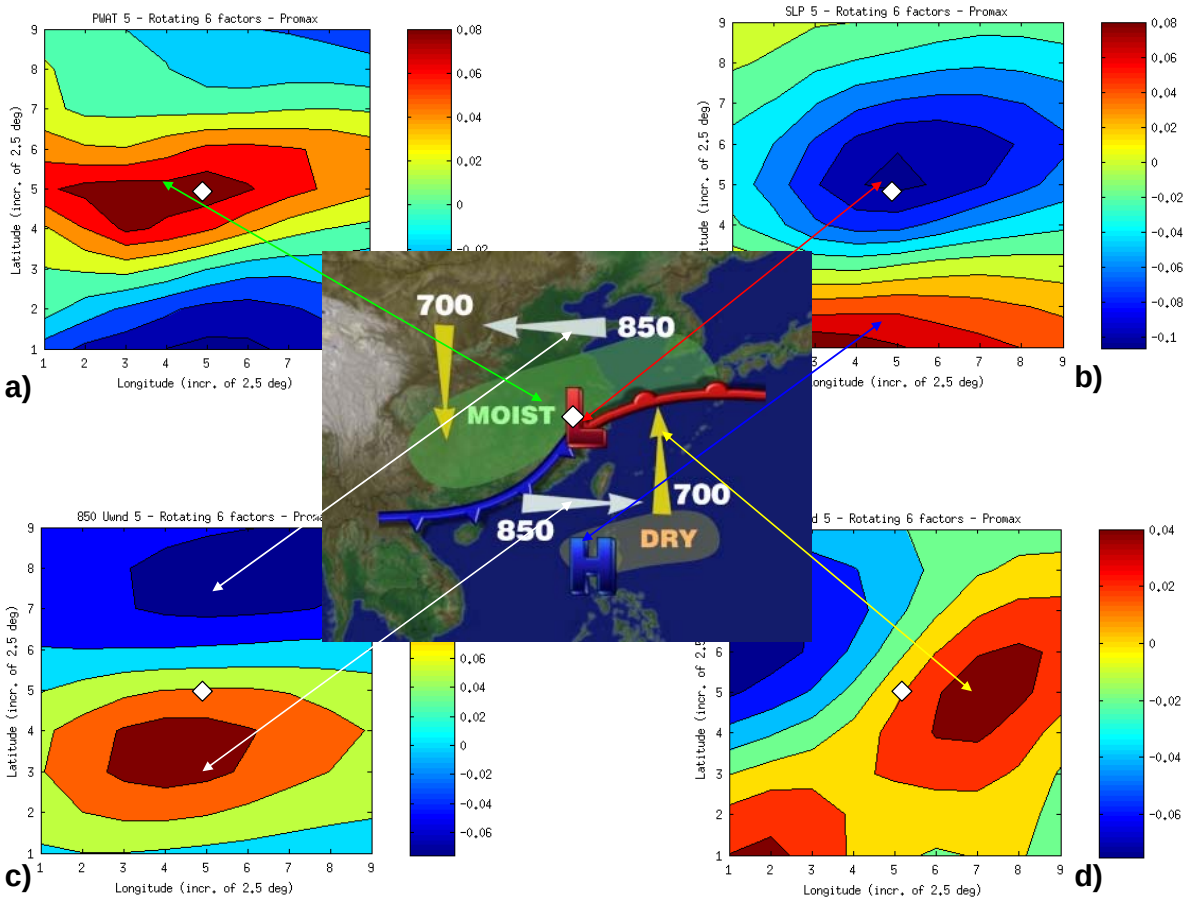

Figure 4.5. The fifth EOF and its representing synoptic pattern, an incipient wave on a front. The heavy rain event is located in the center of each grid at (5,5). Here, (a) displays precipitable water PWAT, (b) displays sea level pressure SLP, (c) displays 850 hPa U-wind, and (d) displays 700 hPa V-wind.

The sixth EOF represents a cold frontal rain band (Figure 4.6) (Djuric 1994). An elongated area of low pressure, or cold front, extends from the northeastern quadrant of the domain southwestward in blue (Figure 4.6b). Along this boundary, high precipitable water (Figure 4.6a) exists and is indicated on the schematic by "MOIST". A westerly component of wind at 850 hPa in red, as well as a southerly component at 700 hPa in red, is located to the east of the heavy rain event. To the northwest of the front, strong high pressure in red (Figure 4.6b) resides in combination with low precipitable water (Figure 4.6a), indicated by "DRY" on the schematic. The high pressure induces an easterly flow at 850 hPa in blue in the western third of the domain (Figure 4.6c) and a northerly flow at 700 hPa in blue in the northwestern quadrant of the domain (Figure 4.6d).

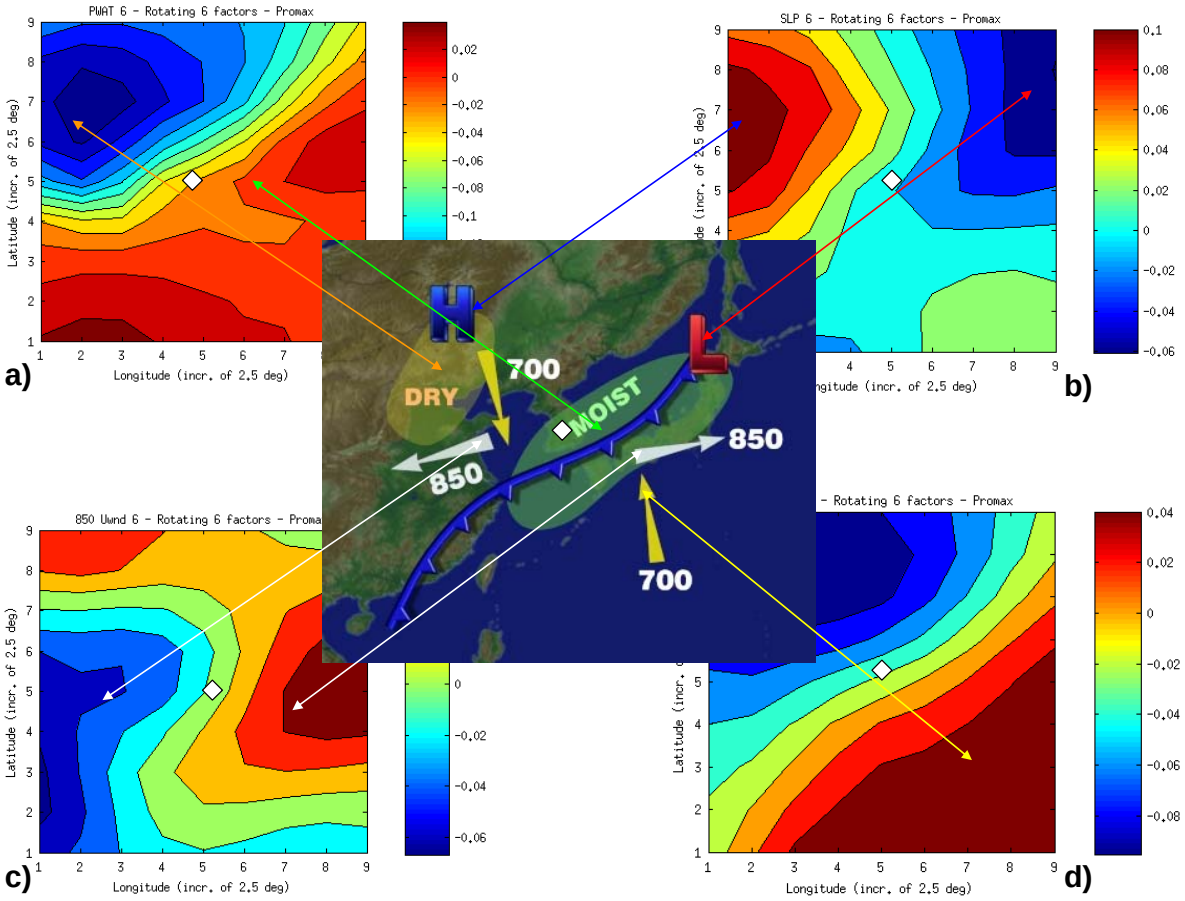

Figure 4.6. The sixth EOF and its representing synoptic pattern, a cold frontal rain band. The heavy rain event is located in the center of each grid at (5,5). Here, (a) displays precipitable water PWAT, (b) displays sea level pressure SLP, (c) displays 850 hPa U-wind, and (d) displays 700 hPa V-wind.

4.2 Event Scores

Event scores, computed and defined in section 3.3.3, determine which EOF(s) best explain each of the 200 heavy rain events. Although event scores demonstrate that multiple EOFs explain one event, there is always one score that is higher than the others. This score represents the primary EOF that explains the event (Table 4.1). The primary EOF represents the synoptic pattern that explains the plurality of the variance in that event.

The events are categorized into three regions, introduced in section 1.2.2: West Coast, Central Continent, and East Coast. The primary patterns that explain the majority of events in the

West Coast region are the second and fifth EOFs, which respectively resemble warm front overrunning and an incipient wave on a front (Table 4.1). Each of these EOFs explains 27% of events that occurred in this region. The second EOF, whose respective pattern is warm front overrunning, also explains the dominant pattern for 33% of the Central Continent events. The third EOF, which represents an open, or developing, stage of a Norwegian Cyclone, and the fifth EOF, which represents an incipient wave on a front, each explain 19% of the Central Continent events. The fifth EOF represents the primary pattern, an incipient wave on a front, and explains 38% of East Coast events. The second EOF, which represents warm front overrunning, explains the dominant pattern for 19% of East Coast events.

Table 4.1. The percentage that explains the dominant pattern for events across three regions: West Coast, Central Continent, and East Coast.

	EOF 1 "Cold Conveyor Belt"	EOF 2 Warm Front Overrunning	EOF 3 Open Stage of a Norwegian Cyclone	EOF 4 Upsloping	EOF 5 Incipient Wave on a Front	EOF 6 Cold Frontal Rain Band
West Coast	9%	**27%**	15%	21%	**27%**	0%
Central Continent	14%	**33%**	**19%**	5%	**19%**	10%
East Coast	6%	**19%**	8%	15%	**38%**	14%

4.3 Statistical Validation of Methodology

To validate the methodology used to extract, build and evaluate the six EOFs, we reconstruct the SA fields for each heavy rain event and compare those with the original SA fields by calculating correlation coefficients. The reconstruction of the SA fields is performed via:

$$\mathbf{R} = \tilde{\mathbf{E}}\, \mathbf{S}_{\mathbf{rot}}, \tag{4.2}$$

where **R** is the matrix of reconstructed SA data, $\tilde{\mathbf{E}}$ is the original matrix of eigenvectors **E** multiplied by the rotation matrix **T**, and $\mathbf{S}_{\mathbf{rot}}$ is the matrix of the rotated scores. An example of the SA field reconstruction is given at the end of this section.

We compare the reconstructed SA fields with the original SA fields for all events using correlation coefficients (Figure 4.7). The vast majority of synoptic signatures are well captured by the six EOFs. A histogram of correlation coefficients shows that 166 of the 200 events, or 83%, have a correlation greater than 0.60, validating our methodology. Ten events have a correlation coefficient of 0.90 or greater and 56 events have a correlation coefficient of 0.82 or greater. One event has a correlation less than 0.30, and 33 events have correlation coefficients between 0.37 and 0.60.

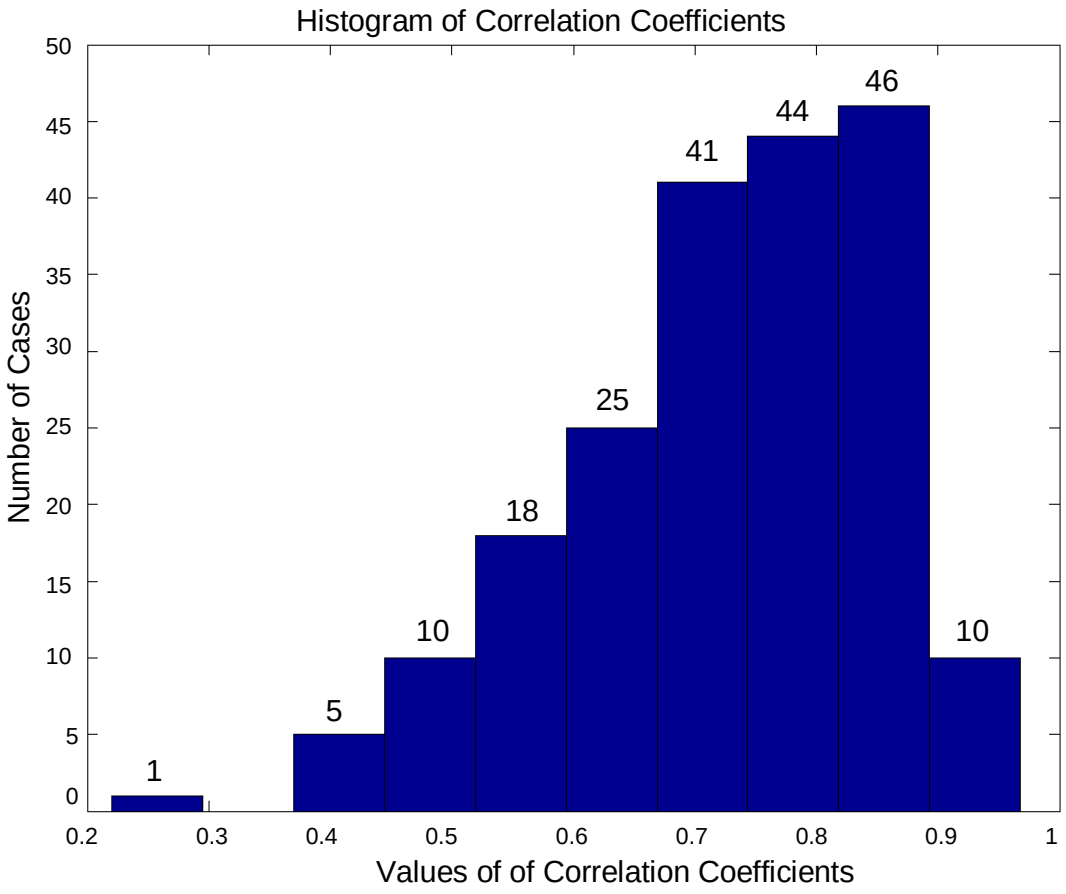

Figure 4.7. A histogram of the correlation coeffients representing the correlation between the original SA fields and those reconstructed using our methodology. Each bin is 0.075 wide. Numbers above each bin represent the number of events that fall in that bin; summing all bin numbers equals 200. Here, 83% of cases have a correlation coefficient greater than 0.60.

Event 70, whose correlation is 0.97, occurred on 25 June 2007 near Leicester, United Kingdom. The reconstructed SA fields (Figure 4.8) closely resemble the original SA fields visually (Figure 4.9). Low sea level pressure in blue (Figures 4.8b, 4.9b) and high precipitable water in red (Figures 4.8a, 4.9a) are to the east of the heavy rain event. Southerlies at 700 hPa in red are to the east of the event with northerlies at 700 hPa in blue to the west (Figures 4.8d, 4.9d). Easterlies at 850 hPa in blue are to the north of the event, and westerlies in red are to the south (Figures 4.8c, 4.9c). According to its scores, event 70 is explained primarily by the first EOF, which resembles a cold conveyor belt pattern that is explained in figure 4.1 at the beginning of section 4.1.

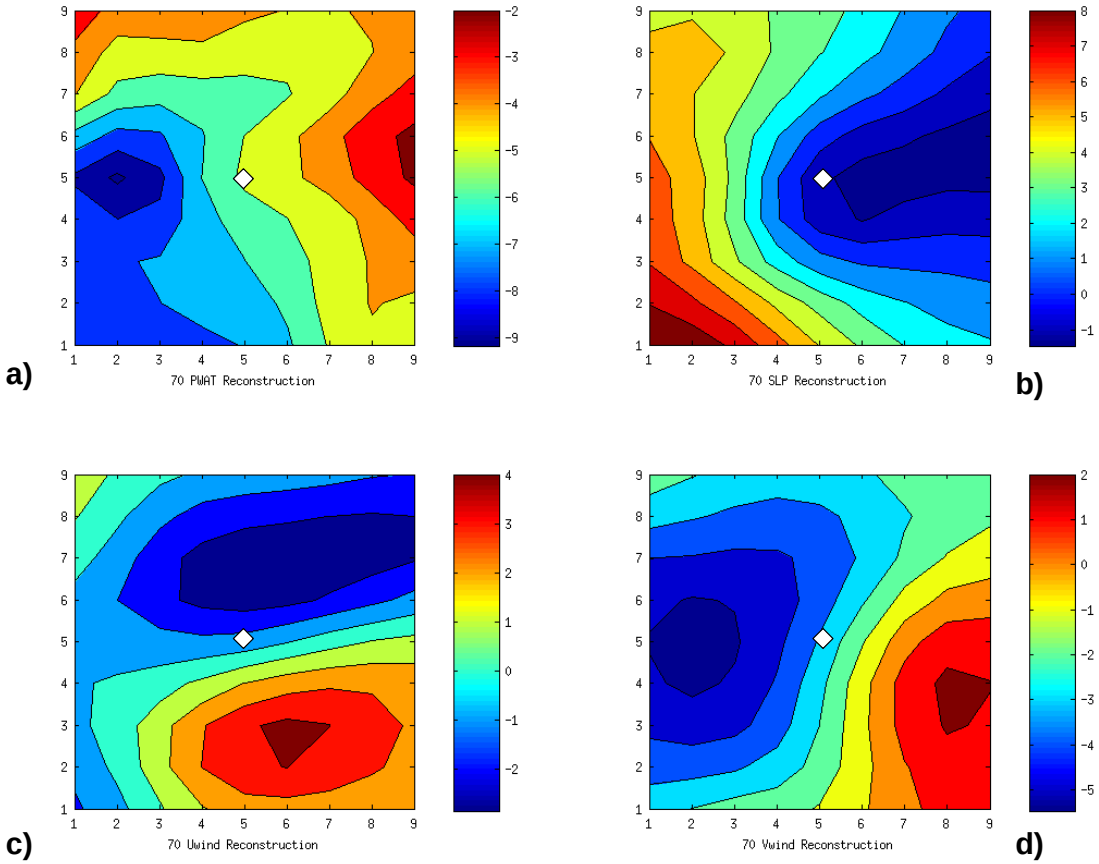

Figure 4.8. The reconstructed SA fields for an event that occurred near Leicester, United Kingdom on 25 June 2007. The heavy rain event is located in the center of each grid at (5,5). Here, (a) displays precipitable water PWAT, (b) displays sea level pressure SLP, (c) displays 850 hPa U-wind, and (d) displays 700 hPa V-wind.

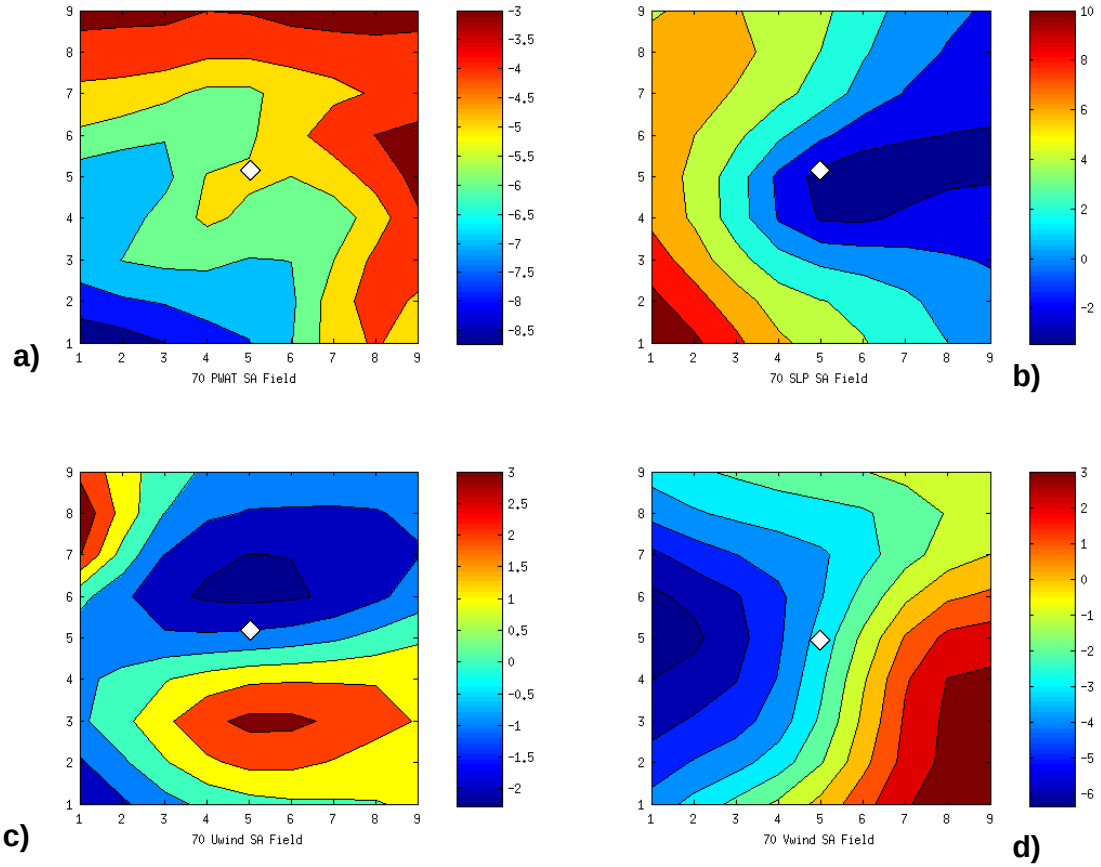

Figure 4.9. The original SA fields for a heavy rain event that occurred near Leicester, United Kingdom on 25 June 2007. The heavy rain event is located in the center of each grid at (5,5). Here, (a) displays precipitable water PWAT, (b) displays sea level pressure SLP, (c) displays 850 hPa U-wind, and (d) displays 700 hPa V-wind.

Chapter 5

Conclusions and Summary

Heavy rain events affect millions of people every year. These events, which often lead to flooding, share common patterns, or fingerprints. This study determines six synoptic patterns that explain the majority of heavy rain events in the mid-latitudes of the Northern Hemisphere using obliquely rotated Empirical Orthogonal Functions EOFs.

Two hundred heavy rain events that led to flooding in the mid-latitudes of the Northern Hemisphere are identified. For each of the 200 events, standardized anomaly SA fields of four atmospheric variables, precipitable water PWAT, mean sea level pressure SLP, 850 hPa U-wind, and 700 hPa V-wind, are extracted from the NCEP/NCAR Global Reanalysis dataset on a 9 by 9 grid centered over the flooding event. Next, unit-length eigenvectors linearly transform the four SA fields so that an Empirical Orthogonal Functions EOFs eigentechnique may be employed.

A subset of the EOFs further condenses the unit-length eigenvectors into a smaller dataset and captures the maximum possible variance from the original SA dataset. To distinguish synoptic patterns that cause heavy rain events, we obliquely rotate the first six eigenvectors according to Promax criterion. These six EOFs are shown to represent six synoptic patterns that explain 61.4% of the variance amongst the 200 flooding events in this study. Six scores, one for each EOF, are calculated for each event to determine the dominant synoptic pattern that induced that particular event.

The dominant pattern in the majority of heavy rain events across the three continents is an incipient wave on a front, the fifth EOF. The second-most dominant pattern that causes heavy

rain events in the Northern Hemisphere is warm front overrunning, the second EOF. The third and fourth EOFs that represent the open stage of a Norwegian cyclone and upsloping patterns, respectively, account for nearly equal amounts of heavy rain events across the mid-latitudes of the three continents. Accounting for the fewest number of flooding events across the Northern Hemisphere are the first and sixth EOFs that represent a cold conveyor belt pattern and a cold frontal rain band, respectively.

To build upon the results of this study, we recommend that the same methodology be used but for standardized anomalies determined from the ECMWF 40-year Reanalysis ERA40 dataset and Japanese 25-year Reanalysis JRA25 dataset. The results of the rotated EOFs derived from the other datasets may be compared with those found in this study. Also, adding more atmospheric fields to the methodology may allow for a more precise synoptic pattern evaluation. Once the synoptic patterns are evaluated and verified using all three datasets, different flood fingerprints may be identified in the predicted model anomaly fields. If fingerprints of heavy rain events can be identified before the event occurs, then life and property loss can be reduced. Finally, this methodology can be tested on other weather hazards, such as heavy snow events and severe weather outbreaks.

APPENDIX A

FLOODING EVENTS USED

Table A.1. Two hundred events from the mid-latitudes of the Northern Hemisphere used in this analysis.

Event Number	Latitude	Longitude	Time/Date	Event Number	Latitude	Longitude	Time/Date
1	31.6	130.5	18Z22Jul2006	38	38.1	128.0	12Z14Jul2001
2	28.2	113.0	12Z23Jun2004	39	37.5	127.0	12Z29Jul2001
3	30.7	104.1	12Z12Jul1981	40	22.3	114.2	00Z18Jun1983
4	22.7	106.1	18Z23Jul1992	41	38.8	127.5	12Z22Oct2006
5	35.0	-93.0	12Z03Dec1982	42	22.3	114.2	06Z11Jun1979
6	39.0	125.8	18Z25Jul1996	43	37.8	-119.5	18Z02Jan2006
7	22.3	114.2	12Z25Jun1985	44	37.5	127.0	00Z07Aug2002
8	37.5	127.0	12Z25Jul1991	45	22.4	114.1	06Z16Jun1993
9	32.0	131.0	00Z07Jul2007	46	29.6	106.5	18Z04Sep2004
10	22.8	120.5	12Z12Jun2005	47	30.7	104.1	00Z16Jun2007
11	32.8	129.9	18Z23Jul1982	48	41.0	-74.0	18Z15Apr2007
12	31.6	130.5	00Z07Jul1993	49	23.1	113.3	06Z20Apr2001
13	22.4	114.1	00Z22Jul1994	50	40.3	21.8	18Z07Oct2006
14	35.9	127.8	12Z01Jul1981	51	22.8	108.3	18Z12Jun2001
15	38.8	127.5	00Z02Aug2001	52	37.9	-84.6	12Z02Mar1997
16	30.3	120.2	06Z25Jun2001	53	37.8	140.5	06Z26Aug1998
17	36.7	117.0	00Z17Jul2004	54	26.6	106.7	12Z23Jun2004
18	23.1	120.8	06Z10Jun2006	55	47.8	-123.6	18Z20Oct2003
19	35.7	139.7	18Z13Aug1999	56	33.5	126.5	06Z12Sep2004
20	30.7	104.0	06Z29Aug2003	57	30.3	120.1	18Z05Sep1999
21	43.3	5.4	00Z02Dec2003	58	23.1	113.3	06Z21May1987
22	34.3	108.9	00Z12Aug1992	59	36.7	117.0	18Z26Aug1987
23	38.8	127.5	18Z09Oct2001	60	46.5	15.0	18Z18Sep2007
24	22.5	114.2	18Z05Apr1987	61	41.8	123.4	06Z25Jul1995
25	28.2	113.0	06Z24Jun2006	62	40.0	125.3	18Z15Jul1996
26	35.1	137.0	18Z11Sep2000	63	38.3	-28.0	18Z28Oct1997
27	22.4	114.1	06Z24Jun2005	64	38.2	125.5	00Z12Sep2004
28	37.5	127.0	06Z11Sep1990	65	37.5	127.0	12Z17Aug2004
29	21.0	108.0	18Z11Sep2003	66	36.5	-90.4	18Z23Sep2006
30	30.6	114.3	18Z01Jul2007	67	22.3	114.1	00Z23Jul1987
31	36.4	127.1	12Z03Aug1997	68	44.0	4.8	00Z09Sep2002
32	42.1	-75.2	12Z28Jun2006	69	38.7	-121.5	00Z11Jan1995
33	40.0	-8.2	12Z22Oct2006	70	52.7	-1.1	12Z25Jun2007
34	22.2	114.2	00Z27Aug1985	71	26.6	106.7	00Z07Jun2000
35	23.1	113.3	12Z11May1982	72	23.1	113.3	06Z29Oct2002
36	28.7	115.9	06Z09May2006	73	22.8	108.3	06Z10Jul2006
37	30.7	104.1	06Z19Sep2001	74	30.7	104.1	06Z07Jul1988

Event Number	Latitude	Longitude	Time/Date	Event Number	Latitude	Longitude	Time/Date
75	23.1	113.3	18Z25Jul1987	121	28.2	113.0	12Z03Aug2002
76	23.1	113.3	06Z21May1998	122	33.5	-94.0	00Z04May1990
77	21.9	104.2	06Z15Apr2004	123	26.0	119.3	12Z20Sep2003
78	43.0	-74.0	12Z30May1984	124	25.0	102.7	18Z28Jul2001
79	28.7	115.9	06Z15May2004	125	40.0	-92.0	00Z23Feb1990
80	26.1	119.3	12Z20May1988	126	30.7	104.1	18Z30Aug1987
81	42.1	-75.1	06Z20Nov2003	127	41.1	-75.5	00Z20Jan1996
82	23.1	113.3	00Z14Apr2000	128	30.7	104.1	06Z14Jun1999
83	33.4	-85.0	06Z18Jun2003	129	25.0	102.7	12Z29Jun2001
84	37.7	-81.5	18Z08Jul2001	130	38.0	23.7	12Z14Jan2001
85	35.9	127.8	00Z04Jul1984	131	37.9	139.0	06Z27Jun2005
86	40.5	39.0	06Z19Jun1990	132	32.8	130.4	00Z29Apr1993
87	29.2	-99.8	12Z21Jul2007	133	25.0	102.7	06Z19Jul2005
88	31.6	130.5	18Z20Jul2003	134	39.0	125.7	00Z06Aug2002
89	37.8	128.3	12Z02Aug2005	135	14.6	121.0	12Z24Aug1993
90	35.0	138.4	18Z11Nov2004	136	43.7	15.9	06Z06Dec2004
91	37.9	139.0	18Z12Jul2004	137	37.7	39.3	00Z02Nov2006
92	43.0	-72.0	12Z05Apr1987	138	26.6	106.7	00Z10May2003
93	41.0	-72.0	00Z06Jun1982	139	37.3	-5.8	18Z02Oct2007
94	29.0	51.6	12Z16Dec2004	140	43.0	-73.0	12Z06May1989
95	37.0	127.0	00Z21Aug1993	141	51.5	44.5	18Z03May1990
96	37.5	127.0	00Z22Jul2000	142	48.5	135.1	12Z04Jun2006
97	30.7	104.1	00Z29Jul1993	143	35.4	136.8	00Z13Aug1998
98	36.2	137.7	18Z22Jul1983	144	37.5	57.3	18Z06May2001
99	47.4	16.0	06Z12Aug2002	145	49.2	19.9	18Z02Jun2006
100	26.0	-80.1	18Z27May2003	146	45.4	12.3	00Z04Jun2002
101	34.3	135.0	18Z30Aug1980	147	43.0	-0.5	18Z26Aug1983
102	35.6	-112.0	06Z11Aug1997	148	43.1	131.9	18Z07Aug2001
103	31.8	117.3	12Z05Jul1987	149	28.2	113.0	18Z11Jun1998
104	28.2	113.0	06Z20Jun2001	150	30.7	104.1	12Z16Jul2000
105	46.5	13.3	18Z29Aug2003	151	30.3	120.2	12Z26Jul2003
106	38.5	106.3	12Z14Jul2006	152	45.9	26.5	18Z05Sep2007
107	38.8	127.5	12Z28Aug1984	153	28.7	115.9	00Z16May2003
108	35.0	-85.0	18Z03May1984	154	29.7	109.1	12Z12Sep2002
109	23.1	113.3	12Z06May2006	155	25.0	102.7	12Z18Jul2006
110	47.3	7.2	12Z09Aug2007	156	34.2	-117.5	00Z26Dec2003
111	36.2	138.3	18Z09Jul1986	157	24.8	121.0	12Z05Aug1997
112	47.1	25.0	12Z13Jun1998	158	39.3	-3.1	06Z23May2007
113	34.7	135.2	00Z27Jun1999	159	42.7	-3.2	06Z07Aug1996
114	37.5	126.9	18Z26Aug1992	160	30.7	104.1	18Z13Jul1989
115	40.0	-79.5	18Z27May1986	161	40.7	-86.2	12Z05May2003
116	35.9	-85.3	06Z07Dec2004	162	30.7	104.1	06Z23Sep2001
117	23.1	113.3	12Z01May2000	163	44.2	-94.0	12Z09Jun2004
118	38.7	-9.1	00Z06Nov2006	164	36.1	138.3	06Z08Jul1988
119	25.0	102.7	18Z28May1984	165	30.6	114.3	18Z23Apr1999
120	37.5	127.0	18Z29Aug2000	166	26.6	52.5	00Z12Jan2002

Event Number	Latitude	Longitude	Time/Date	Event Number	Latitude	Longitude	Time/Date
167	29.6	106.5	06Z30Apr2001	184	26.6	106.7	12Z12Jun2006
168	31.6	130.5	00Z06Aug1993	185	38.8	-83.8	00Z12Sep2006
169	34.3	108.9	06Z02Oct2005	186	35.0	72.0	18Z02Aug1983
170	60.4	5.3	00Z14Aug2003	187	37.0	-122.0	00Z01Jan1982
171	48.9	11.4	00Z14Jan2004	188	29.0	77.0	00Z02Jul1990
172	40.3	40.9	18Z01Jul2006	189	41.8	123.4	18Z15Aug2005
173	41.0	-104.5	00Z02Aug1985	190	41.6	24.7	18Z05Jun2004
174	23.1	113.3	06Z01Jun2001	191	38.8	31.2	06Z13Sep1999
175	25.0	102.7	00Z01Oct2002	192	45.7	126.6	12Z09Jun2005
176	32.0	-83.0	00Z06Apr1982	193	36.6	138.2	06Z05Dec1996
177	30.7	104.1	18Z11Aug1991	194	30.8	-96.6	00Z10May2004
178	34.3	108.9	12Z14Jul2000	195	23.1	113.3	18Z09Sep1991
179	52.2	21.0	00Z17Jul2001	196	30.7	104.1	00Z04Oct1981
180	36.0	103.8	12Z28May2005	197	26.6	106.7	12Z04Jun2004
181	33.0	-85.0	18Z09Nov1990	198	39.0	125.8	18Z30Jun2005
182	25.0	102.7	00Z24Sep1991	199	47.2	19.5	06Z05Mar2001
183	43.6	1.4	18Z12Nov1999	200	37.1	25.2	00Z19Oct2006

APPENDIX B

DERIVATION OF ROTATED SCORES USING A LEAST-SQUARES APPROACH

If **D** is the original standardized anomaly data in a 324X200 matrix, **E** is the 324X6 matrix of the first six unit-length eigenvectors, and **S** is the 6X200 matrix of unrotated scores, then it follows that

$$\mathbf{D = ES.}$$

To obtain the rotated scores, we use the least-squares approach,

$$\mathbf{D = \tilde{E}\, S_{rot}}$$

where $\mathbf{\tilde{E}} = \mathbf{ET}$, **T** is the 6X6 rotation matrix, and $\mathbf{S_{rot}}$ is the 6X200 matrix of rotated scores. It follows that

$$\mathbf{\tilde{E}^{-1}D = S_{rot}.} \tag{B.1}$$

Because (B.1) is difficult to compute and verify numerically, we find an equivalent $\mathbf{S_{rot}}$ that is more readily calculated. First, multiply each side of (B.1) by $\mathbf{\tilde{E}^T\tilde{E}}$:

$$\mathbf{\tilde{E}^T D = \tilde{E}^T\tilde{E}\, S_{rot}.}$$

Therefore, it follows that

$$\mathbf{(\tilde{E}^T\tilde{E})^{-1}\,(\tilde{E}^T D) = (\tilde{E}^T\tilde{E})^{-1}(\tilde{E}^T\tilde{E})\, S_{rot},}$$

which leads to the more readily calculated expression for $\mathbf{S_{rot}}$,

$$\mathbf{(\tilde{E}^T\tilde{E})^{-1}\,(\tilde{E}^T D) = S_{rot}.} \tag{B.2}$$

REFERENCES

Cattell, R. B., 1966a: The scree test for the number of factors. Multivariate Behavioral Research, 1(2), 245-276.

DeGaetano, A.T., and S.M. Jessup, 2008: A statistical comparison of the properties of flash flooding and nonflooding precipitation events in portions of New York and Pennsylvania. Wea. Forecasting, 23, 114-130.

Djuric, D., 1994: *Weather Analysis.* Prentice-Hall, 304 pp.

Dunteman G. H., 1989: *Principal Components Analysis*. SAGE Publications, Newbury Park, CA, 95 pp.

Glickman T. S., Ed., 2000: *Glossary of Meteorology.* 2d ed. Amer. Meteor. Soc., 855 pp.

Grumm, R.H., and R. Hart, 2001: Standardized anomalies applied to significant cold season weather events: preliminary findings. *Wea. Forecasting*, **16**, 736–754.

Hendrickson, A. E. and P.O. White, 1964: Promax: a quick method to oblique simple structure. *Brit. J. Stat. Psych.,* **17,** 65.

Kaiser, H.F., 1958: The Varimax criterion for analytic rotation in factor analysis. *Psychometrika,* **23,** 187.

Kalnay, E., M. Kanamitsu, R. Kistler, W. Collins, D. Deaven, L. Gandin, M. Iredell, S. Saha, G. White, J. Woollen, Y. Zhu, A. Leetmaa, R. Reynolds, M. Chelliah, W. Ebisuzaki, W. Higgins, J. Janowiak, K. Mo, C. Ropelewski, J. Wang, R. Jenne, and D. Joseph, 1996: The NCEP/NCAR 40-Year Reanalysis Project. *Bull. Amer. Meteor. Soc.*, **77**, 437–471.

Lorenz, E., 1956: Empirical orthogonal functions and statistical weather prediction. Tech. Rep. 1, Statistical Forecasting Project, Department of Meteorology, Massachusetts Institute of Technology, Cambridge, MA, 49 pp.

Maddox, R.A., C.F. Chappell, and L.R. Hoxit, 1979: Synoptic and mesoscale aspects of flash flood events. *Bull. Amer. Meteo. Soc.,* **60**, 115-123.

Onogi, K., J. Tsutsui, H. Koide, M. Sakamoto, S. Kobayashi, H. Hatsushika, T. Matsumoto, N. Yamazaki, H. Kamahori, K. Takahashi, S. Kadokura, K. Wada, K. Kato, R. Oyama, T. Ose, N. Mannoji and R. Taira, 2007: The JRA-25 Reanalysis. J. Meteor. Soc. Japan, **85**, 369-432.

Petterssen, S., 1941: *Introduction to Meteorology*. 1st ed. McGraw-Hill, 236 pp.

Richman M. B., 1986: Rotation of principal components. J. Climatol., 6, 293–335.

Root, B., P. Knight, G. Young, S. Greybush, R. Grumm, R. Holmes, and J. Ross, 2007: A fingerprinting technique for major weather events. *J. Appl. Meteor. Climatol.*, **46**, 1053–1066.

Thurstone, L.L., 1947: *Multiple Factor Analysis.* The University of Chicago Press, Chicago, IL.

Wilks, D.S., 1995: *Statistical Methods in the Atmospheric Sciences.* Academic Press, New York, 467pp.